Planetary Helicopter Brownout Simulation of Ingenuity using a Eulerian Dust Transport Model

Denis-Gabriel Caprace*, Ethan Baker†, Patricia Ventura Diaz‡, Seokkwan Yoon§
NASA Ames Research Center
Moffett Field, CA, USA

Ingenuity has sustained an astonishing 72 flights on Mars. The small helicopter proved that non-terrestrial powered flight is possible, even on planets with thin atmospheres. Future planetary rotorcraft will be bigger and heavier to accomplish new scientific and exploratory goals. For example, the Dragonfly mission will send a rotorcraft of the size of a regular car to explore Titan. However, on dusty planets, the increase in rotor thrust due to increased weight poses a potential challenge. Dust clouds could form during take-off and landing due to rotor wash, a phenomenon referred to as brownout. This work evaluates the effectiveness of existing numerical simulation models in predicting the severity of this phenomenon for planetary rotorcraft. We compare the output of a CFD-based dust mobilization model with Ingenuity flight data gathered using image processing techniques. The simulation results suggest that the sensitivity of the wall friction velocity to the rotorcraft height may be lower than previously assessed. We further evaluate the sensitivity of the total mass of mobilized dust to other model parameters such as the sandblasting efficiency and the saltation threshold velocity. Finally, we discuss the limitations of this comparison due to uncertainty in both the observational and the numerical model.

I. Nomenclature

α = Sandblasting efficiency [$\mathrm{m^{-1}}$]

b = Inter rotor distance [m]

d = Diameter of saltating particle [m]

Δx = Mesh resolution [m]

F = Flux of mobilized dust normal to the ground [$\mathrm{g\,m^{-2}\,s^{-1}}$]

g = Gravitational acceleration [$\mathrm{m\,s^{-2}}$]

Adapted from AIAA Paper 2024-4341 presented at the AIAA Aviation Forum, Las Vegas, NV, July 29 – August 2, 2024.

*Oak Ridge Associated Universities, NASA Postdoctoral Program fellow, AIAA member.
†Intern, Computational Physics Branch.
‡Science and Technology Corporation, AIAA member. Corresponding author: patricia.venturadiaz@nasa.gov
§NASA Advanced Supercomputing Division.

h	=	Height above the ground calculated as the distance between the ground and the bottom rotor plane [m]
Q	=	Saltation mass flux parallel to the ground [$\mathrm{g\,m^{-1}\,s^{-1}}$]
R	=	Rotor radius [m]
ρ	=	Ambient density [$\mathrm{kg\,m^{-3}}$]
ρ_s	=	Density of solid particle [$\mathrm{kg\,m^{-3}}$]
ρ_p	=	Density of particulate matter in the flow [$\mathrm{g\,m^{-3}}$]
θ_0	=	Blade pitch angle [°]
ν	=	Fluid kinematic viscosity [$\mathrm{m^2\,s^{-1}}$]
$\mathbf{u}$	=	Flow velocity vector [$\mathrm{m\,s^{-1}}$]
$\mathbf{u}_g$	=	Particle fallout velocity vector due to gravity [$\mathrm{m\,s^{-1}}$]
u_{*it}	=	Impact threshold velocity [$\mathrm{m\,s^{-1}}$]
u_{*ft}	=	Fluid threshold velocity [$\mathrm{m\,s^{-1}}$]
W	=	Far field rotor-induced velocity [$\mathrm{m\,s^{-1}}$]
Ω	=	Rotor rotational speed [$\mathrm{s^{-1}}$]

II. Introduction

Planetary exploration with aerial vehicles, as improbable as it seemed only a few decades ago, has now proven to be a formidable opportunity to increase the yield of science missions to extraterrestrial worlds [1]. Ingenuity —the small helicopter deployed on Mars by NASA's Perseverance rover and the first ever human device to achieve powered flight outside Earth's atmosphere (Fig. 1)— has demonstrated the feasibility of operating a rotorcraft on another planet [2]. Originally intended as a mere proof of concept, Ingenuity's extraordinary longevity allowed NASA teams to build extensive operational experience with significant scientific impacts [3]. The whole endeavor further demonstrated the validity and maturity of the models used in planetary rotorcraft design [4]. This success opens the door to many future expeditions to Mars and other frontiers with rotorcraft of increasing size and complexity. Upcoming NASA missions will further push the boundaries set by Ingenuity, such as the Mars Science Helicopter with a 15 times heavier rotorcraft [5], or the even more ambitious Dragonfly mission to Titan [6].

In any case, operating a rotorcraft in dusty environments presents a number of challenges and risks that must be assessed during the design of the vehicle [7]. In particular, the phenomenon of brownout can occur when the rotorcraft hovers close to the ground. The unsteady and complex airflow generated by the rotor, called rotorwash, can interact with particulate matter lying on the ground, resulting in their uplifting and the development of a possibly dense cloud of "dust". On Earth, brownout can put helicopter operations at risk by blocking the pilot's visibility or reducing situational awareness. This naturally occurs during take-off and landing, where, coincidentally, precise control

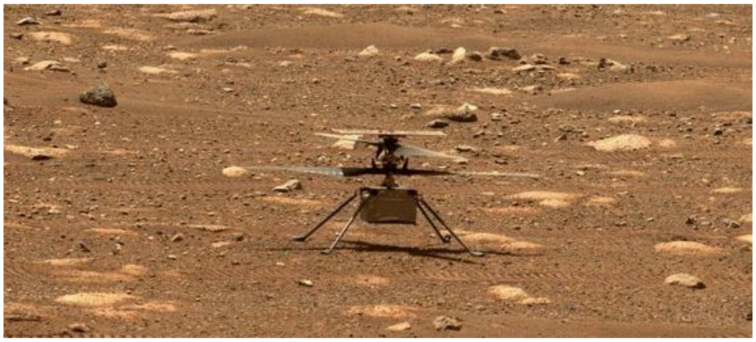

Fig. 1 Ingenuity on the surface of Mars. Credit: NASA/JPL-Caltech/ASU.

is most vital. A similar danger exists for planetary rotorcraft, which would use vision-based sensors or instruments. Most notably, Ingenuity relied on cameras to plan and execute navigation and landing site selection [8]. Since dust mobilization usually increases with the rotor disk loading (and, generally speaking, with the vehicle mass) [9], this topic needs to be accounted for in the design of increasingly heavy planetary aerial vehicles that will carry payloads and perform more complex scientific missions [10, 11]. Additional areas of concern related to brownout are dust erosion and/or accumulation, which, for example, could perturb the functioning of critical mechanisms (such as rotor blades or swashplates) or cause a premature drop in the performance of solar arrays [12]. Another potential hazard comes from the possibility of energetic discharge of particles electrically charged by impingement of suspended material on the rotors [13]. The risks associated with each of these aspects must be carefully assessed for future flights on Mars and beyond. Notably, the Dragonfly mission to Titan is expected to operate in a regime where brownout could be a factor, which has prompted a number of investigations [14, 15]. However, obtaining reliable predictions of the brownout phenomenon is challenging due to the complex nature of the processes involved and their sensitivity to a large number of environmental parameters.

Brownout is caused by the interaction between rotorwash and particle bed that triggers natural mechanisms of sediment mobilization such as saltation bombardment, aerodynamic lifting, and disaggregation [16]. In many natural processes, saltation bombardment is dominating [16–18]. Dedicated experiments confirmed that it is also the mechanism driving the emission of dust during brownout on Earth [19, 20]. Saltation refers to the movement of sand particles along the surface that move in a series of irregular, discontinuous jumps under the influence of wall shear stress. Bombardment, sometimes also called sandblasting, occurs when these particles enter in contact with the surface and transfer momentum to smaller dust particles, resulting in their ejecting in the flow as illustrated in Fig. 2. A distinctive feature of rotorwash flows is the presence of coherent vortical structures originating in blade tip vortices. Experiments have shown that these structures can lead to local shear stress concentration, lower pressure, particle vortex trapping, recirculation or reingestion of particles, and their interaction with flow turbulence, all of these affecting dust emission [21–23]. Consequently, the details of the rotorwash flow, which can be turbulent and complex [24, 25], have a pronounced

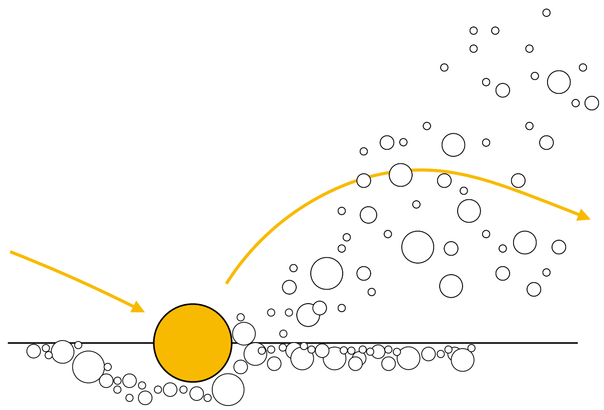

Fig. 2 Illustration of the saltation bombardment process. A saltating sand particle (yellow circle) emits dust (black circles) through sandblasting on the ground surface.

influence on the efficiency of the sediment mobilization. This renders the brownout modeling task complex.

Substantial work has been done on numerical modeling of helicopter brownout. Computational fluid dynamics (CFD) is generally used to simulate the flow physics of the carrier phase. The solid particle phase can be accounted for by means of Eulerian or Lagrangian discretizations. In the former, the particulate matter is handled as a continuous phase with a density that is solved for on the computational grid, as in [26, 27]. In this approach, the emission of dust corresponds to a wall-normal flux that models the effect of saltation bombardment and any other relevant processes. The accuracy of the computation therefore relies on this model to introduce realistic amounts of dust in the flow [28]. On the other hand, the Lagrangian discretization enables tracking of individual particles [29–31] and the force acting on each of them can be directly calculated. The Lagrangian discretization has the advantage that the condition for dust mobilization at the boundary can be fully simulated, including the details of saltation bombardment. However, the associated computational cost may prevent the direct simulation of saltation bombardment in configurations involving a complete rotorcraft. In such conditions, the uplifting of particles from the wall also needs to be parameterized [32] or modeled [33]. Even so, the cost associated with the tracking of a large number of particles may become intractable for a full rotorcraft [34]. For a given total number of physical dust particles, the number of numerical particles (and the associated cost) can be reduced by introducing mesoscale modeling whereby each numerical particle represents a cluster of multiple physical particles [35, 36].

Considering the various models involved in both Lagrangian and Eulerian frameworks, validation based on experimental data has been undertaken. Flight test campaigns have been conducted on Earth with full-size helicopters, and have demonstrated the sensitivity of dust lifting to rotor disk loading [37, 38], advance ratio [39], and rotor height [40]. Optical techniques were developed to track the position of the dust cloud [41] and to assess the severity of the associated loss of visual reference [42]. Due to the difficulty of controlling the conditions of field experiments and the limited number of available measurements, most previous validation efforts have been limited to comparing the

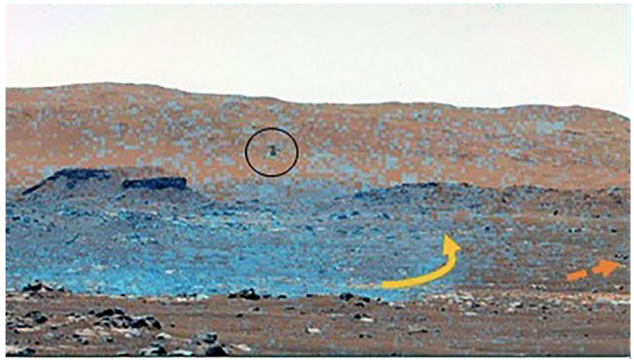

Fig. 3 Sample image of Ingenuity, processed to compute the mass of mobilized dust. The yellow arrow symbolizes dust advection and the orange arrow shows the wind direction. Ingenuity is circled in black. CC-BY Lemmon et al. [47]

spatial extent of the dust cloud [31, 43], without going into the details of the dust density distribution or total mass of lifted dust. A good qualitative agreement was generally reported despite the impossibility to verify all parameters of the experiment. In some cases, validation of numerical results was complemented with wind tunnel observations at model scale to compare them on a phenomenological basis [44, 45] . However, one must be careful when extrapolating experimental data from model-scale to full-scale as it is unlikely that such data has been obtained in full similarity. Among the 15 non-dimensional numbers that pertain to sediment transport, Perrotta et al. [46] hypothesized that those involving wall friction have a stronger influence on sediment mobilization as they control the mechanisms of dust emission. For example, aerodynamic lifting through pressure effects may be important at model scale but not at full scale. The same principle should apply when characterizing the environment on Earth versus other planets [14].

At Mars, the conditions are also prone to aeolian sediment transport, as was demonstrated by data recently collected *in situ* by multiple probes [48]. Among the available data, images of Ingenuity operation in ground proximity have been video recorded and show the occurrence of dust kick-ups. This paper aims to investigate the potential for using such observational data in conjunction with numerical simulation to infer environmental parameters. Specifically, a dedicated analysis of Ingenuity's flights by Lemmon et al. [47] has provided data on the mass of mobilized dust during several flight sequences. The mass has been estimated based on images recorded by the Perseverance rover with its cameras filming the helicopter and its environment (Fig. 3). The images have been processed by comparing pixel brightness with a mean reference and relating changes in opacity to dust density. This dataset provides a unique opportunity to verify models against real-world data in an extraterrestrial environment.

In this paper, we combine existing simulation and modeling techniques that have been previously employed for Earth conditions to simulate the Ingenuity helicopter on Mars during brownout. We calculate the mass of dust mobilized for various parameters of the models, and we compare our results with the observational data. Finally, we discuss the agreement and discrepancies in regard to the assumptions made in the numerical models and in the image processing technique.

III. Methods

The present work relies on a numerical approach that, as far as dust modeling is concerned, presents strong similarities with existing Eulerian representations [26, 28]. A vortex particle-mesh (VPM) method is employed to simulate the flow around Ingenuity. This CFD method is a medium-fidelity tool that enables long rotorcraft simulations at an affordable computational cost, a critical feature that further enables parametric analyses. The CFD code determines the velocity field in the surroundings of the rotorcraft, including its interaction with the ground. An equation is added for the transport of a scalar that represents the density of dust, with a dedicated source term and boundary conditions that model the physics of saltation bombardment. This dust emission model and the transport equation have both been implemented in the code specifically for this work and allow us to track the distribution and total mass of mobilized dust as a function of time in the simulations. This data is eventually compared with the observations.

A. Computational Fluid Dynamics Solver

The VPM method solves the incompressible Navier-Stokes equations in their vorticity-velocity formulation. It utilizes a hybrid Lagrangian-Eulerian discretization. On the one hand, vortex particles are employed to solve the flow advection. On the other hand, the stretching and diffusion are solved on a background Cartesian grid through the use of fourth-order finite differences. Sub-grid scale modeling is also performed by applying a filtering operation on the grid information. The resulting method is known to have low dissipation and dispersion errors [49], while being computationally efficient (including on massively parallel architectures) [50]. The aerodynamics of the wings and rotors are modeled using lifting lines, which take care of shedding the appropriate vorticity in the vicinity of the lifting surfaces [51]. For conciseness, we refer to [50–52] for a detailed description of the method, and specifically to [53] for the description of the sub-grid scale model. Multiple rotorcraft applications have been explored with the VPM method [54–57, 57, 58], with consistent validation where possible.

A schematic of the computational domains used in this work is shown in Fig. 4. The model of Ingenuity is placed at the center of a square ground plane and hovers at a constant height h, the distance between the bottom rotor and the ground. The lateral and top domain boundaries are set to unbounded conditions. Of specific interest to this work, the ground is modeled as a flat surface. To this end, a no-slip boundary condition is imposed at the bottom of the Eulerian domain. Because the resolution of the background grid is uniform in the whole domain, the wall boundary layer is actually under-resolved, but the numerical method remains stable. Previous experience showed that this under-resolved boundary condition is capable of capturing realistic rotorwash flows. In fact, this approach was verified against detached eddy simulation considering the flow around a single rotor in ground effect [59]. Additional comparisons with experimental and other numerical results showed favorable agreement.

For the purpose of this work, we introduce the capability of the model to compute an instantaneous wall shear stress, τ_w. Because the wall boundary layer is under-resolved, a few assumptions are introduced in order to extrapolate the

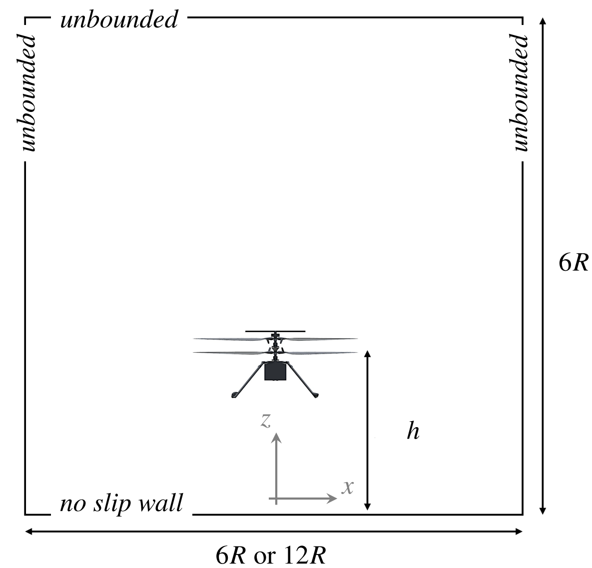

Fig. 4 Computational domain for the VPM simulations.

velocity profile in the near-wall region. First, the flow is assumed to be fully turbulent at every point of the ground surface. This assumption is supported by wind-tunnel observations of rotorwash [25]. Further assuming a smooth surface, we use the law of the wall by Reichardt [60],

$$u^+ = \frac{1}{\kappa}\log(1+\kappa z^+) + (C - \kappa\ \log(\kappa))(1 - e^{-z^+/11} - (z^+/11)\, e^{-z^+/3}), \tag{1}$$

with the conventional definition of wall variables $u^+ = {}^{u}/_{u_*}$ and $z^+ = {}^{(z\,u_*)}/_{\nu}$, and where the boundary layer parameters used in the following are the von Kármán constant $\kappa = 0.383$ and $C = 4.25$. The equation is solved for the friction velocity $u_* = \sqrt{\tau_\text{w}/\rho}$ at every time step of the simulation and for all grid points of the ground surface. The value of u is set to the norm of the instantaneous velocity vector projected in a plane parallel to the ground at a given distance to the wall z, typically one grid point above the surface, assuming that this location is within the log region of the boundary layer. The so-obtained local instantaneous u_* is a measure of the wall shear stress as could be obtained by other wall-modeled LES techniques of the literature.

B. Helicopter Model

We developed a model of the Ingenuity helicopter for the VPM simulation environment. The model consists of two counter-rotating rotors with two blades each (Fig. 5). The blade planform geometry was taken from publicly available data [61, 62] and is shown in Fig. 6. We assumed all blades were made with the `CLF5605` airfoil along the entirety of their span. Since the aerodynamics of the blades are represented with a lifting line approach in the VPM simulations, we generated a full set of 2D polar data using XFOIL [63]. The lifting line is fed with tabulated lift and drag coefficients obtained as a function of angle of attack, Reynolds, and Mach numbers. The instantaneous force at each blade section is determined from a table look up using local conditions. This way, the compressibility affecting the lift and drag of the blade is accounted for in the model.

All the simulations presented in this article were performed under the same Martian conditions. A temperature of 200 K was assumed. The viscosity was calculated using Sutherland's law. The corresponding environmental and rotor parameters are summarized in Tables 1 and 2. While the rotors' rotational speed was set to its nominal value, the collective pitch angle was manually adjusted so that the total thrust balances the weight of the vehicle (for a mass of 1.8 kg).

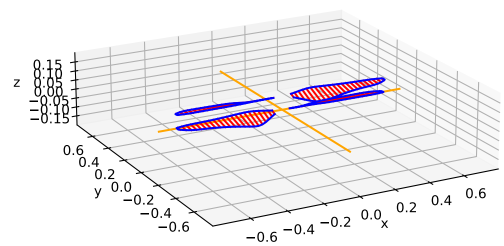

Fig. 5 3-D geometry of Ingenuity's rotor model.

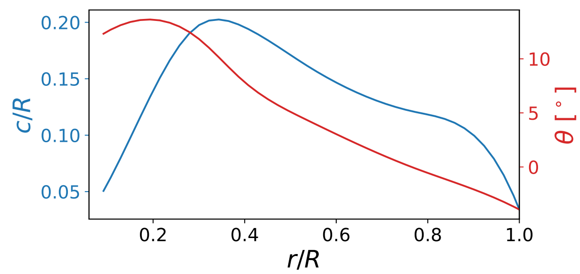

Fig. 6 Chord and twist distributions of each blade.

C. 3-D Dust Mobilization Model

We support the derivation of Phillips and Brown [26] and the assumption that the forces acting on typical dust particles result in a near equilibrium between aerodynamic and gravitational effects (i.e., low Stokes number). They arrive at an equation for the transport of a monodisperse particle phase with given particle properties, represented as a continuum of density ρ_p,

$$\frac{\partial \rho_\mathrm{p}}{\partial t} + (\mathbf{u} + \mathbf{u}_\mathrm{g}) \cdot \nabla \rho_\mathrm{p} = S_\mathrm{p} + D_\mathrm{pt} \nabla^2 \rho_\mathrm{p}, \tag{2}$$

with $\mathbf{u}$ the flow velocity, $\mathbf{u}_\mathrm{g}$ the particle fallout velocity, S_p a source term, and D_pt an effective mass diffusivity constant. The fallout velocity is modeled as in [26],

$$||\mathbf{u}_\mathrm{g}|| = \frac{\nu}{d} \left(\sqrt{25 + 1.2 d_\star} - 5 \right)^{1.5}, \tag{3}$$

where the dimensionless particle diameter is defined as $d_\star = d \left(g(\rho_\mathrm{s} - \rho)\rho^{-1}\nu^{-2} \right)^{1/3}$. The effective diffusivity is computed as $D_\mathrm{pt} = \nu_\mathrm{t}/\mathrm{Sc}_\mathrm{t} + D_\mathrm{p}$, where ν_t is the flow turbulent viscosity provided by the sub-grid scale model, Sc_t is the turbulent Schmidt number, and D_p is the molecular diffusivity. Our estimate for the latter is based on the Stokes-Einstein-Sutherland equation and suggests that it is negligible compared to the sub-grid scale contribution.

The entrainment of dust particles in the flow is accounted for through S_p that is only active at the first grid point above the wall. As is common to any numerical model with a Eulerian treatment of particulate matter, the physical processes causing mobilization are here modeled. Since it is believed to be dominant during brownout, saltation bombardment is the only mechanism we consider. The model utilized in this work has strong similarities with other implementations found in Earth system models (e.g., [64]), mesoscale atmospheric models (e.g., [65]), and macroscale simulations of helicopter brownout [28, 34].

Saltation occurs when relatively large sand particles or dust aggregates are mobilized and enter a rolling-hopping motion with a direction mostly parallel to the ground, as illustrated by the yellow particle and arrows in Fig. 2. The onset of the phenomenon depends on the balance between the gravity force, the aerodynamic drag, and the interparticle cohesion force acting on the particles [66]. A description of this balance in terms of wall friction has led to the definition of two thresholds [67, 68]. From a still situation, saltation is initiated when the friction velocity reaches the saltation fluid threshold, $u_{*\mathrm{ft}}$. After saltation has been initiated, it can be sustained as long as the friction velocity remains larger than the impact threshold velocity, $u_{*\mathrm{it}}$. On Mars, a typical value for the ratio $u_{*\mathrm{it}}/u_{*\mathrm{ft}}$ is 0.1 [66]. This value is used as a fixed parameter for the present work.

The saltation mass flux, Q, is conventionally defined as the horizontal flux of particles participating in saltation and integrated across the height of the saltation layer. It is expressed in $\mathrm{kg\,m^{-1}\,s^{-1}}$. Correlations relating Q to the shear stress at the wall and various environmental parameters were developed from observations [66, Table 1]. We utilize the widely accepted model developed by Kawamura [69] and later refined by White [70],

$$Q = 2.61 \frac{\rho}{g} {u_*}^3 \left(1 - \frac{u_{*\mathrm{it}}^3}{{u_*}^3}\right) \left(1 + \frac{u_{*\mathrm{it}}}{u_*}\right), \tag{4}$$

where $u_{*\mathrm{it}}$ is the impact threshold velocity.

Sandblasting is a consequence of saltation [71]. When the saltating particles enter in contact with the ground surface, these particles can transfer momentum to dust particles on the ground and dislodge them, resulting in their ejection into the flow. The mass flux of particulate matter entering the flow as a result of sandblasting is noted F and expressed in $\mathrm{kg\,m^{-2}\,s^{-1}}$. Observations have suggested that F is correlated to Q [17, 72, 73], supporting the theory that sandblasting results from a transfer of kinetic energy between the saltating particles and the ejected ones —a transfer that is characterized by a certain conversion rate or efficiency [66]. Consequently, a common modeling approach is to consider that F represents a fraction of the saltation mass flux, hence calculated as

$$F = \alpha\, Q, \tag{5}$$

where α is referred to as the sandblasting efficiency [74] and has units of $\mathrm{m^{-1}}$.

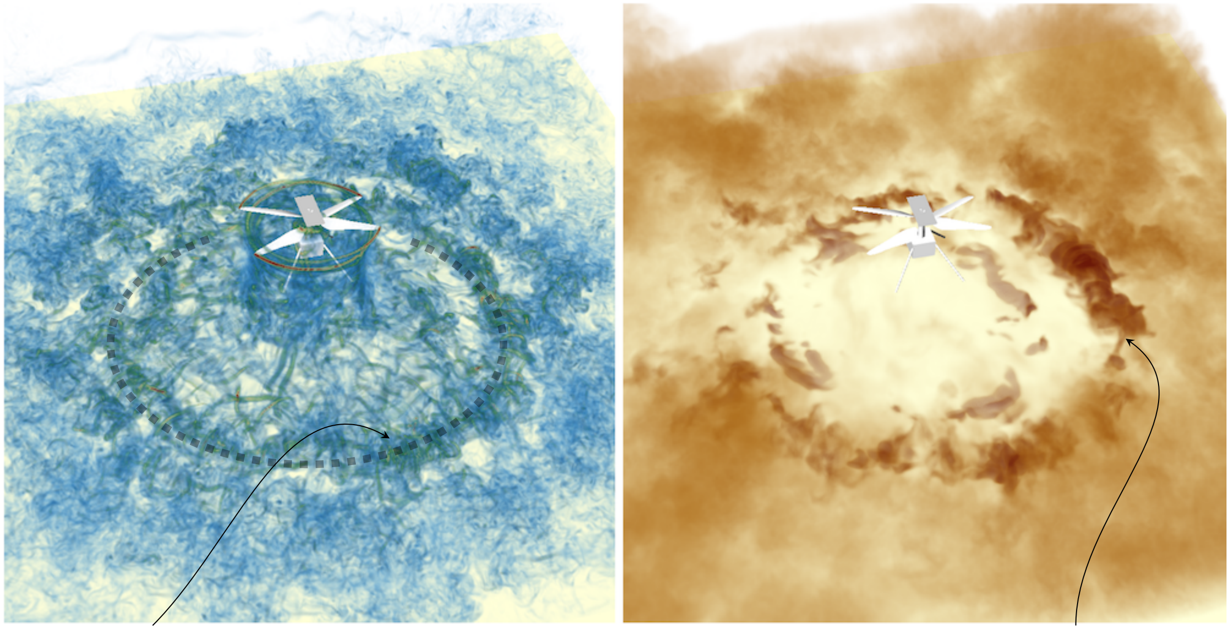

Fig. 7 Visualization of a snapshot result from the simulation of Ingenuity hovering at $h/R = 2$, showing the vorticity field on the left and the density of dust on the right, by volume rendering.

Finally, the source term in Eq. (2) is obtained as

$$S_{\mathrm{p}} = \begin{cases} F/\Delta x & \text{if } u_* \geq u_{*\mathrm{ft}} \\ 0 & \text{otherwise} \end{cases} \tag{6}$$

Since F is a mass flux per unit area, we rather impose it as a source term in the volume. The source is active only when the local friction velocity exceeds the fluid threshold.

An instantaneous snapshot of the simulation of Ingenuity in hover above a flat ground is shown in Fig. 7. The vorticity from the rotor forms ring-shaped coherent vortical structures that travel along the ground surface. The dust mobilization model responds to the flow velocity and produces more dust in regions of high wall shear stress.

Regarding the estimation of mobilized dust, the total mass is calculated as the integral of the dust density in the whole computational domain,

$$M(t) = \int \rho_{\mathrm{p}}(\mathbf{x})\, \mathrm{d}\mathbf{x}. \tag{7}$$

The finiteness of the domain has implications on the computed mass that are discussed at the end of this paper. The simulations in this study assume a monodisperse particle field. The numerical values for the main model parameters are given in Table 3.

Table 1 Environmental properties.

$g =$	3.721	$\mathrm{m\,s^{-2}}$
$\rho =$	0.020	$\mathrm{kg\,m^{-3}}$
$\nu =$	5.65×10^{-4}	$\mathrm{m^2\,s^{-1}}$

Table 2 Rotor operating conditions.

$R =$	0.605	m
$b =$	0.073	m
$\Omega =$	2 500	RPM
$\theta_0 =$	4.0	°

Table 3 Dust properties.

$\rho_s =$	2 000	$\mathrm{kg\,m^{-3}}$
$d =$	1.4	µm
$\mathrm{Sc_t} =$	10	–
$\lvert\lvert \mathbf{u}_g \rvert\rvert =$	0.030	$\mathrm{m\,s^{-1}}$

IV. Outwash Velocity Induced by Ingenuity in Hover

When a rotorcraft hovers above a flat surface, the flow induced by the rotor(s) is redirected from downwash in the region right underneath the rotors to outwash along the surface. In the region directly above the surface, a so-called wall jet forms with a velocity mainly pointing along the outward radial direction. The velocity profile across the thickness of the jet has been measured experimentally for various model-scale and full-scale rotorcrafts on Earth (see, e.g., [75] and references therein). It has been shown that, when established, the jet adopts a self-similar profile that appears to be universal, where the similarity variables are $u_{\max}$ and $z_{1/2}$. The former is the maximum velocity in the jet, and the latter is the height at which the velocity reaches half of the maximum value. This self-similar behavior was also obtained in CFD simulations (see, e.g., our previous work [59]).

The time-averaged velocity profile in the jet is calculated for Ingenuity. The results are obtained from VPM simulations in a domain of size $6R \times 6R \times 6R$. The background Cartesian grid uses a uniform resolution corresponding to $\Delta x/R = 1/48$ unless otherwise specified. To simulate hover, the Ingenuity rotorcraft model is placed at a given height above the surface and at the center of the domain in the other two directions. All simulations were run on NASA's Pleiades Supercomputer hosted by the NASA Advanced Supercomputing (NAS) Division at NASA Ames Research Center. Nominally, a single case would run for about 8 hours on 216 Intel Haswell processors.

The resulting velocity profiles at a radial distance of $r/R = 1.5$ from the center of the rotors are shown in Figs. 8 and 9. In the former, the curves are normalized with rotor variables, where W is the far field rotor-induced velocity (see also Section V.A). In the latter, the similarity variables are used. Increasing hover height leads to decreasing maximum velocity in the jet at a fixed radial location. On the other hand, the jet width increases until at least $h/R = 4$. The self-similar profile is observed for rotor heights under $h/R = 3.5$ but starts deviating as the rotor height further increases. Changes in $u_{\max}$ and $z_{1/2}$ are also quantified in Fig. 10.

To verify the consistency of the numerical modeling, the effect of the grid resolution on the calculated outwash velocity profile was evaluated. Three simulations of increasing resolutions were performed with $\Delta x/R = 1/24, 1/32$, and $1/48$. Results are shown in Fig. 11. The maximum velocity in the jet shows a converging behavior while $z_{1/2}$ also saturates. Even though only three resolutions are considered here, these results and previous experience with the code in

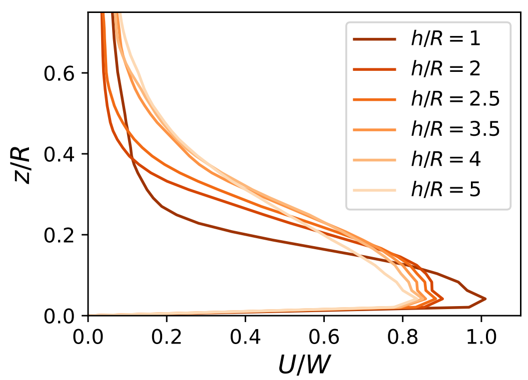

Fig. 8 Outwash velocity profile at a distance of $r/R = 1.5$ normalized with rotor variables.

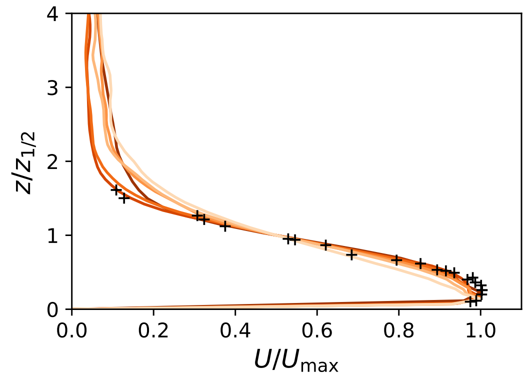

Fig. 9 Outwash velocity profile at a distance of $r/R = 1.5$ normalized with wall jet variables, overlayed with full-scale helicopter data (+) from [76].

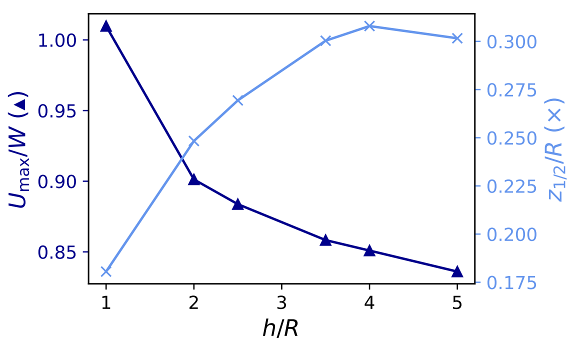

Fig. 10 Effect of height on the wall jet variables in the simulations of Ingenuity in hover ($\Delta x/R = 1/48$).

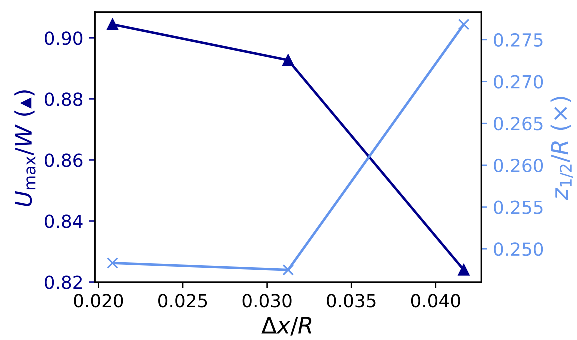

Fig. 11 Effect of grid resolution on the wall jet variables in the simulations of Ingenuity in hover at $h/R = 2$.

similar configurations give us confidence in the consistency of the numerical modeling.

V. Friction Velocity on the Ground

The wall jet induced by the rotor causes friction on the ground surface. The friction velocity, a measure of the intensity of the wall shear stress, is a crucial quantity in the modeling of dust mobilization. As shown in Section III.C, the normal flux of dust mass at a given location on the surface scales with ${u_*}^3$ when the friction velocity is above the flow threshold velocity. This section compares the values of u_* calculated in the simulation with the predictions of an analytical model.

The numerical setup in this section is identical to the previous section. The friction velocity at every grid point on the ground surface is recorded during the simulations. The data collected during the first second (or equivalently, about 40 rotor revolution periods) is discarded to let the initial transient evacuate from the simulation domain and reach an established regime. Statistics are then collected over the following 2.5 s, that is, over about 100 rotor revolutions. Distributions of the friction velocity are obtained for various radial locations by aggregating data over the azimuthal direction and time. The mean u_* and a confidence interval are also extracted. We compare these values with the prediction of the analytical model presented hereafter.

A. Rabinovitch Model and Comparison to Simulation Results

In computing the friction velocity, Lemmon et al. [47] use the model described by Rabinovitch et al. [14], which we recall here for completeness. This model was derived as a quick-to-evaluate engineering tool to assess the feasibility of performing aeolian experiments with rotorcrafts on other planets. Although this model is of lower fidelity than CFD computations, it was developed from first principles and remains a useful tool for conceptual studies. Therefore, we offer comparisons between our results and the model predictions, together with possible improvement suggestions.

The Rabinovitch model predicts a nominal τ_w by analogy with the analytic solution of an axisymmetric laminar stagnation flow,

$$\tau_\mathrm{w} = 1.3120\,\rho\,\nu^{1/2}\,a^{3/2}\,r, \tag{8}$$

where r is the radial distance from the stagnation point, and a is a parameter that represents a characteristic strain rate at the wall, i.e., the ratio between a characteristic flow velocity and a characteristic length. Rabinovitch et al. propose to define the latter as

$$a_\mathrm{original} = \frac{W + u_\text{tip vortex}}{2h}, \tag{9}$$

where $W = 2\sqrt{T/(2\rho A)}$ is the far field rotor-induced flow velocity from momentum theory with T the rotor thrust and A the rotor swept area. Because blade tip vortices are recognized to locally increase shear stress, the strain rate includes a correction which augments the average flow induction W with a nominal vortex-induced flow velocity estimated as $u_\text{tip vortex} = 3.66T/(\sigma\rho A\Omega R)$, with σ the rotor solidity. Since Eq. (8) predicts that the shear stress increases monotonously with r, a characteristic value is taken at the location $r/R = 1$, which is meant as a representative value for the shear stress induced by a rotorcraft on the ground.

We compare the analytical prediction from Rabinovitch et al. [14] with the CFD-predicted friction velocity for Ingenuity's rotor system hovering at a height of two rotor radii. Figure 12 shows histograms of the friction velocity distribution at various radial distances from the rotor axis, in blue. The associated confidence interval is constructed between the 0.5^th and the 99.5^th percentile. These percentiles were chosen as statistically significant estimates of the lowest and highest likely friction velocity. The mean of the distributions is also shown as a function of the radial distance. Similar information is presented in gray, showing a friction velocity based solely on the radial component of the velocity above the wall, i.e., the radial shear stress. The comparison between total and radial shear stresses indicate that the radial component dominates for $r/R > 1$, whereas the tangential shear component becomes significant in the inboard region. Furthermore, the sign change of the mean radial friction denotes the presence of a recirculation region beneath the rotor, as expected from experiments [24].

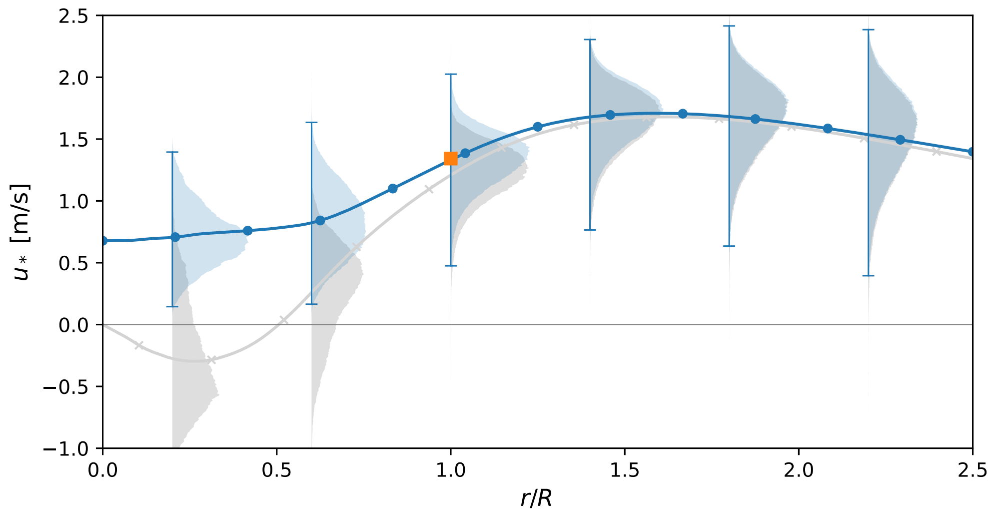

Fig. 12 Friction velocity on the ground simulated for Ingenuity hovering at $h/R = 2$, as a function of the radial distance to the rotor axis: distributions of u_* ( ), their average ( ), and 0.5–99.5% confidence interval ( ) from the simulations. Distributions ( ) and averages ( ) for a friction velocity based on the radial shear only. Prediction of the original model by Rabinovitch et al. [14] ( ).

Quite remarkably, the Rabinovitch model prediction agrees almost perfectly with the mean u_* at $r/R = 1.0$. We note that the mean u_* from the CFD continues to increase with the radial distance and peaks at around $r/R = 1.5$. The analytical model thus predicts a slightly lower friction velocity than the peak average u_* calculated in the CFD.

While the average friction velocity is valuable information, it does not reflect the unsteady character of the rotor-induced wall jet in which the effect of coherent vortical structures is predominant. Previous model scale studies have exposed that large amounts of dust are released under the action of these coherent flow features that originate in rotor blade tip vortices or the product of their merging [20, 44]. As highlighted previously, such structures are indeed identified in the 3-D vorticity and dust visualization in Fig. 7 (see also Section VI). The passage of these vortical structures is associated with coherent fluctuations of the shear stress which can be characterized through the evolution of the instantaneous friction velocity. For small helicopters, dust thus appears to be released in bursts. Recent experimental evidence on Earth has suggested that coherent vortical structures could break down earlier in the wake of heavy rotorcraft [77], typically, before reaching the ground vicinity. Whether this leads to a more continuous release of dust in the flow remains to be determined. Regardless, it is desirable to investigate the effect of more or less coherent turbulent structures on the time history of the friction velocity.

From a statistical perspective, the blue histograms in Fig. 12 indeed reveal that higher friction velocities than the average are likely to occur. For example, when examined as a function of r/R, the envelope of the highest likely u_* keeps growing until approximately $r/R = 1.8$ where it reaches a value about 1.5 times higher than the peak average, then slowly decreases. At radial distances larger than $r/R = 1$ —that is, outside of the recirculation region and in the wall jet—, the distributions can be fairly well approximated with a skewed normal probability density function (PDF). A fit of the results is provided in the Appendix. It reveals that the skewness parameter remains approximately constant in the established wall jet and confirms that the distribution is skewed towards the higher friction velocities. This is a significant departure from the PDF of wall shear stress observed in regular turbulent channel flows [78] and boundary layers [79], where the skewness is towards the lower values. The shape of these PDFs may have implications on the modeling of saltation and sandblasting, which usually assumes the flow above the wall to be an established turbulent boundary layer. Additionally, the highest likely u_* is related to the strength of the vortical structures. All in all, the statistical description provides more information that could be exploited to better parameterize brownout in future models, in comparison with established saltation thresholds. We further discuss this in Section VII.

To simplify our descriptions in the remainder of this article, we focus on the peak mean u_* (i.e., the maximum along the radial distance), and the peak 0.5^{th} and 99.5^{th} percentile u_*. These three quantities are meant to be representative of the more complex shear stress probability density function as a function of the radial coordinate.

B. Sensitivity to Rotor Height

To assess the sensitivity of the friction velocity to the rotor height, several simulations have been performed with Ingenuity hovering at various heights. The results are summarized in Fig. 13.

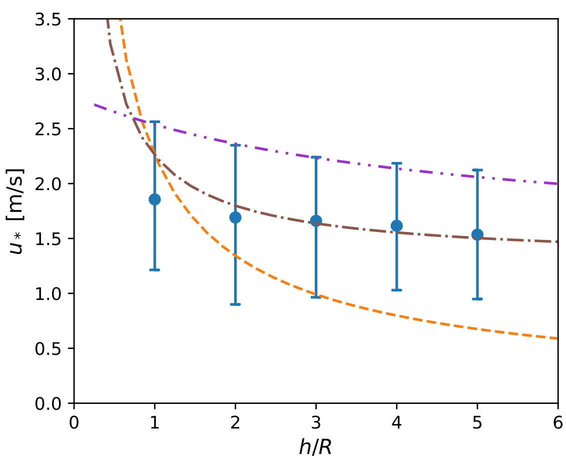

Fig. 13 Friction velocity on the ground predicted by the simulations of Ingenuity hovering at various heights: peak mean u_* (●), and range between peak 0.5% and peak 99.5% percentile friction velocity (⌶). Predictions by Rabinovitch et al.'s original model (- -), our modified version (-·-), and fit of the highest likely u_* (-··).

Both the peak 99.5^{th} percentile (noted $u_*^{99.5^{\text{th}}\text{pct}}$ from here on) and the peak mean friction velocity exhibit a lower sensitivity to height compared to the original formulation of the analytic model. This can be problematic when one aims to use the analytic model to determine the flow threshold velocity from observational data, as proposed by Lemmon et al. [47].

We revisit the analytical model by Rabinovitch et al. in light of these results. First, we note that, as opposed to a regular jet, a rotorcraft wake usually does not experience a significant expansion over the first couple of diameters downstream of the rotor. Instead, experiments (e.g., [80]) and CFD (e.g., [81]) show that the area under the rotor where the induced velocity is significant remains relatively constant, or even contracts close to the rotor. While an expanding jet impinging on a surface would induce a strain rate that decreases proportionally to the inverse of its height, we argue that a rotor wake would not, as long as the rotor is close enough to the surface. This motivates the modified expression

$$a_{\text{modified}} = \frac{W}{2R} + \frac{u_{\text{tip vortex}}}{2h}, \tag{10}$$

where contribution of W to a is independent of h. On the other hand, the influence of the vortex-induced velocity still scales with the inverse of the height. This effect is justified by the growth in size of the vortical structures as a function of their age, which tends to decrease their maximum induced velocity. Figure 13 shows the prediction of this modified model as a function of the rotor height. It better captures the trend in the peak mean friction velocity for heights above $h/R \geq 2$. We expect Eq. (10) to be valid up to $h/R \approx 6$. At greater heights, the wake may start to expand. This is consistent with the downwash velocity predicted by Hohler [82], which is thought to remain constant within the first three to four diameters of the rotor and then decrease. Despite the favorable agreement with the data at hand, the validity of Eq. (10) would need to be evaluated on other rotorcrafts and over a larger range of heights.

In addition, we are interested in modeling the maximum likely friction velocity. We propose to adapt again the expression of the strain rate to establish a fit of $u_*^{99.5^{\text{th}}\text{pct}}$ calculated in the simulation. When the wake ages, coherent structures form as a result of the merging of blade tip vortices and subsequent vortex interactions. Through these interactions, the average size and the circulation of the vortical structures grow. Since intermittent high friction velocities are caused by the passage of these structures, we define a new strain rate a_{fit} based on the maximum strain induced by a coherent vortex. This maximum strain corresponds to the maximum vortex-induced flow velocity $u_{\text{coherent vortex}}$ divided by its core radius σ_v,

$$a_{\text{fit}} = b_1 \frac{u_{\text{coherent vortex}}}{\sigma_v}, \tag{11}$$

where b_1 denotes a fitting parameter. We choose to model the vortex-induced velocity at the location of the core radius using the point vortex formulation,

$$u_{\text{coherent vortex}} = \frac{1}{2\pi} \frac{\Gamma_v}{\sigma_v}. \tag{12}$$

We model the circulation of the coherent structure as

$$\Gamma_v = \Gamma_0 \left(1 + \frac{1}{b_2} \frac{h}{W}\right), \tag{13}$$

where the initial circulation corresponds to the tip vortex circulation $\Gamma_0 = 2.3\frac{W^2}{2}\frac{\bar{c}}{R\Omega\sigma}$, the same expression as in Rabinovitch et al.'s original model with $\bar{c}$ the blade mean chord and σ the rotor solidity. Equation (13) models the growth in circulation of the coherent structure as a function of their age. The factor h/W represents the age of the structure when it reaches the vicinity of the ground, while b_2 (with units of seconds) is a fitting parameter to specify the time it takes for the structure to double in circulation. Finally, the growth in the average core size of the coherent structure is modeled as a typical vortex growth,

$$\sigma_v = \sqrt{r_0^2 + 4\alpha_L \nu_{\text{eff}} \frac{h}{W}}, \tag{14}$$

where $r_0 = 0.1\bar{c}$ is the assumed initial tip vortex core size, $\alpha_L = 1.25643$ is Lamb's constant, and ν_{eff} is an effective diffusivity. The latter is also a fitting parameter.

The result of the fit with parameters $b_1 = 0.21$, $b_2 = 0.25$ s, and $\nu_{\text{eff}} = 0.02$ m^2 s^{-1} is shown in Fig. 13. The fitted curve captures the trend in ${u_*}^{99.5^{\text{th}}\text{pct}}$. Similarly, the modified model of Eq. (10) better reproduces the calculated peak mean u_* compared to Rabinovitch et al.'s original model which overestimates the sensitivity of u_* to height. The possible implications of this overestimation on the assessment performed by Lemmon et al. [47] are discussed in the next section.

Finally, we stress that the difference between peak mean u_* and maximum likely u_* is a measure of the width of the wall shear stress distribution. Instead of ${u_*}^{99.5^{\text{th}}\text{pct}}$, one could parametrize the evolution of the moments of the distribution (e.g., mean, standard deviation, and skewness, as shown in the Appendix). Accounting for the stochastic character of the wall shear stress could help refine engineering models, for example, in determining the likelihood of exceeding the saltation threshold. However, such a model extension is outside of the scope of the present work.

VI. Lifted Dust during Take-Off

We focus on the total mass of dust mobilized during take-off of the Ingenuity rotorcraft. Our aim is to compare independent predictions of dust mobilization by the numerical simulations of this work and the dataset obtained by Lemmon et al. [47]. Although desirable, further comparison with other experimental data (e.g., collected on Earth) is impractical due to inconsistencies in rotor configurations and flight conditions between our simulations and existing datasets. Concerning the data on Ingenuity, the spatial distribution of dust would be hard to compare (even qualitatively) due to the limited resolution and the 2-D character of the observed images. Still, a quantitative comparison is possible for the total mass of dust mobilized over time. This integral diagnostic allows us to highlight the potential sources of discrepancy between the results of our numerical model and the data sourced in image processing. We identify three main quantities that significantly affect the dust model predictions: the friction velocity on the ground, the sandblasting efficiency, which controls the vertical flux of dust, and the threshold velocities. This section illustrates the sensitivity of the mass of lifted dust to these three parameters.

Regarding the numerical setup, the flow is again initialized as quiescent, and the counter-rotating rotors start spinning impulsively at their nominal rotational velocity at $t = 0$. We aim to emulate the take-off phase to match the configuration observed in reality. However, for simplicity, the kinematics of the vehicle are omitted. Instead, the rotorcraft is held at a fixed position in hover. The size of the domain is increased to $12R$ in the lateral directions while maintaining $6R$ vertically. To allow faster turnaround times, the simulations are run on a coarse mesh of resolution $\Delta x/R = 1/24$.

Due to the impulsive character of the start up in both the simulation and in reality, a starting vortex forms as a result of the merging of early tip vortices. As observed in Fig. 14, the starting vortex travels downwards and interacts with the dust on the surface. The wake then continues to entrain more particles from the ground, contributing to a growing cloud of dust. Around $t = 0.6$ s, some dust starts to exit the simulation domain under the effect of the rotor outwash velocity. Eventually, the simulation reaches an established condition in which dust is lifted from the ground, is entrained in the outwash flow, and eventually leaves the computational domain.

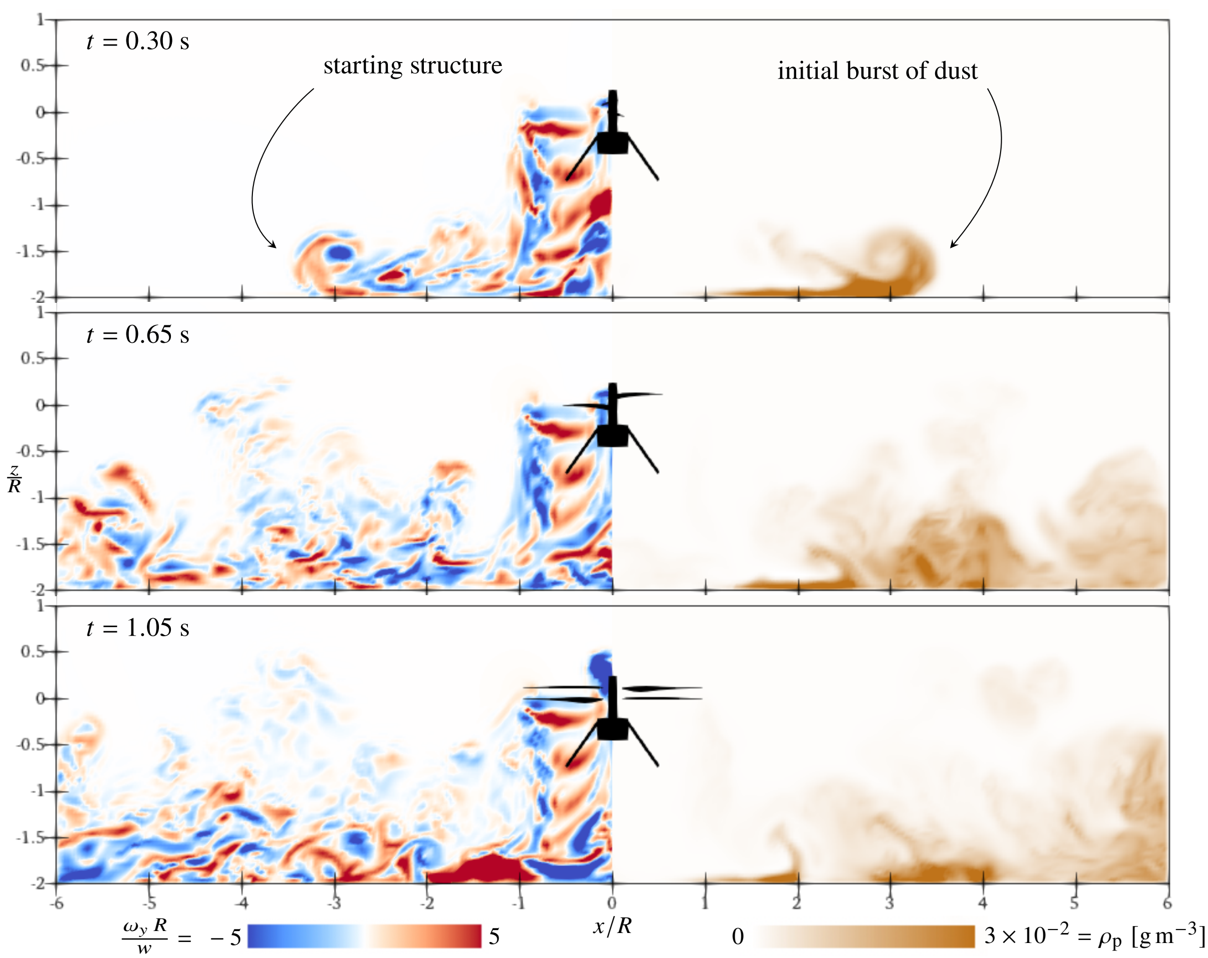

Fig. 14 Instantaneous snapshots of the plane-normal vorticity (left) and the density of dust (right) in a cross section of Ingenuity's simulation with $h/R = 2$ and $\Delta x/R = 1/24$.

For the baseline case presented hereafter, the lower rotor is at a height of two rotor radii above the ground (as shown in Fig. 14). The sandblasting efficiency is set to $f = 0.004\ \mathrm{m}^{-1}$, the ratio $u_{*\mathrm{it}}/u_{*\mathrm{ft}}$ is assigned the value 0.1, and the threshold velocity $u_{*\mathrm{ft}} = 0.54\ \mathrm{m\,s}^{-1}$. The latter is set to match the estimation by Lemmon et al. [47] from their observation combined with the original Rabinovitch model.

From visual inspection of Fig. 14, dust is present in a cylinder of height $2R$ and radius $6R$. The corresponding volume is approximately $V = 50\ \mathrm{m}^3$, and the side projection area $A = 24R^2 = 8.8\ \mathrm{m}^2$. Assuming an optical depth τ of the side projection between 0.01 and 0.1 and a dust density of $\beta = 1.6\ \mathrm{g\,m}^{-2}$ per unit opacity (as reported by Lemmon et al.), the dust mass in the simulation $M = \beta A \tau$ should range netween 0.14 and 1.40 g. The corresponding average dust density should be $\rho_\mathrm{p} = 3 \times 10^{-3} \ldots 3 \times 10^{-2}\ \mathrm{g\,m}^{-3}$. This estimation is in good agreement with the dust density reported in Fig. 14.

A. Effect of Sandblasting Efficiency

The vertical flux of mobilized dust, Eq. (5), drives the total amount of mobilized dust as it is directly proportional to the only source of dust in our model. Therefore, the sandblasting efficiency is a key parameter of the model that, however, incurs a high uncertainty.

On Earth, studies have measured α in wind tunnels (e.g.,[83–85]) or in the field (e.g., [74, 86–88]). The experimental techniques often involve the measurement of the concentration at different heights, the assumption of an established boundary layer, and an analogy between the vertical flux of particulate matter and the turbulent momentum flux in the near-wall region. The obtained measurements range between 10^{-5} and $10^{-2}\ \mathrm{m}^{-1}$ and appear to be sensitive to a large number of environmental parameters, but also to the friction velocity. In spite of this variability, various attempts have been made in the literature to parametrize α using empirical relations (e.g., [89]) or physics-based approaches (e.g., [18, 90, 91]). However, the ensuing models do not generalize well to the many soil properties and particle size distributions at different locations on Earth [92], let alone, on another planet. For this reason, we restrict our study to a sensitivity assessment of the lifted mass of dust to the value of α.

To illustrate the effect of the sandblasting efficiency, we compute the mass of lifted dust in our simulations for various values of α, and we compare the results to Lemmon et al.'s processing output. The computed mass of dust mobilized during take-off is shown in Fig. 15 as a function of time.

The mass of mobilized dust calculated in the simulation reflects the vortex dynamics of the impulsively started hovering rotor discussed above. In the initial phase, the mass grows rapidly under the effect of the starting structure that progressively covers a larger area until it reaches the domain boundary. The mass saturates after the starting vortex exits the domain and maintains itself at a relatively constant amount in the established phase. This amount is primarily a function of the size of the computational domain. This is an obvious limitation of our fixed size domain approach.

A similar behavior is seen in the data observed during the take-off of two different flights that Ingenuity performed

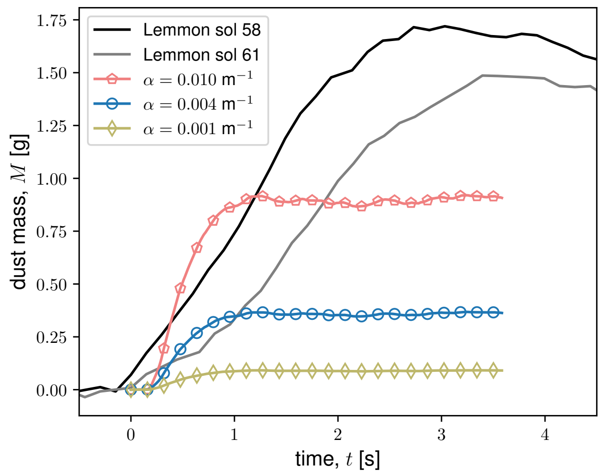

Fig. 15 Lines with symbols: computed mass of mobilized dust as a function of time for three different values of the sandblasting efficiency, α. Lines without symbols: observational data from two different Martian sols [47]. The starting vortical structure leaves the computational domain between t = 0.6 s and 1 s.

on Martian sol 58 and sol 61. In these two instances, the rotorcraft ascends vertically up to a height of about 8 R (16 R, respectively) during the first 6 seconds (8 s, resp.) of the sequence and then maintains hover for at least 10 seconds. The initial phase is characterized by a growing cloud of dust, the mass of which increases linearly over the first 1.5 to 2.0 seconds. The observed amount of dust then saturates as the cloud starts leaving the field of view of the camera. The observed mass then decreases as the cloud dissipates while Ingenuity is still in hover. Because it hovers at heights, the friction velocity associated with its wake at the end of the ascent is smaller than during the first instants of the take-off sequence. Dissipation and transport win over production, which allows the total dust mass to decrease.

In the simulation results as well, the slope of the initial growth in dust mass is roughly linear and scales with the sandblasting efficiency. At a given hovering height, the total mass of dust in the established phase is proportional to α as expected. Considering the difference in size of the computational domain with respect to the field of view of the camera and the difference in the kinematics of the rotorcraft, it is inconsequential to compare the mass of dust mobilized in the established phase between the observational and the simulation data. However, the parameters in the initial instants of the transient phase are similar enough to enable a more quantitative comparison of the lifted mass of dust and its rate. We note that for the chosen values of $u_{*\mathrm{ft}}$, an α of about 0.004 m^{-1} gives a favorable agreement of the slopes. Going further than this simple argument based on orders of magnitude is complicated by the uncertainty on both $u_{*\mathrm{ft}}$ and α.

B. Effect of Threshold Velocities

The fluid and the impact threshold velocities are environmental parameters subject to a relatively large uncertainty because they depend on a large number of soil properties including particle size and shape distributions, moisture content, surface roughness, cohesiveness, and more [20]. Many experimental studies have measured these threshold in various conditions, as reviewed by Kok et al. [66]. Subsequently, models of the threshold velocities have been proposed, such as the widespread model by Shao and Lu [93]. However, observations made in Martian conditions have shown unexpected behaviors [94], possibly related to relatively low atmospheric pressure. Pressure effects may indeed affect the balance of forces acting on sand grains resting on the surface [46], but the conditions in which this becomes significant are usually not observed during natural erosion on Earth. Incidentally, it has been hypothesized that pressure effects may manifest during brownout due to the low pressure associated with tip vortices [22] or high velocity jets [95]. A correction of the model by Shao and Lu was proposed by Leishman et al. [7] to account for pressure, but its effectiveness was never evaluated. Furthermore, it must be noted that existing measurements and models of threshold properties usually imply an established boundary layer above the wall. Whether these threshold velocities are valid in a rotorwash with dominant coherent vortex structures remains to be determined. Considering all these sources of uncertainty and the fact that soil properties for the observational data at hand are mostly unknown, we limit our effort to a study of the sensitivity of our results to $u_{*\mathrm{ft}}$.

We evaluate the effect of the fluid threshold velocity on the mass of mobilized dust. Considering Lemmon et al.'s estimation of $u_{*\mathrm{ft}} = 0.54\ \mathrm{m\,s^{-1}}$ as the baseline, Fig. 16 shows that a threefold increase in $u_{*\mathrm{ft}}$ leads to a threefold decrease in dust mass. However, a fourfold increase in $u_{*\mathrm{ft}}$ leads to the almost complete suppression of the dust production at the wall. The total mass of dust is thus highly sensitive to the threshold velocity, which, similarly to α, can cause orders of magnitude changes in the calculated value. Therefore, it is impossible to discriminate the effect of α and $u_{*\mathrm{ft}}$ solely from the observed integrated mass of mobilized dust since both parameters can induce large variations on the result.

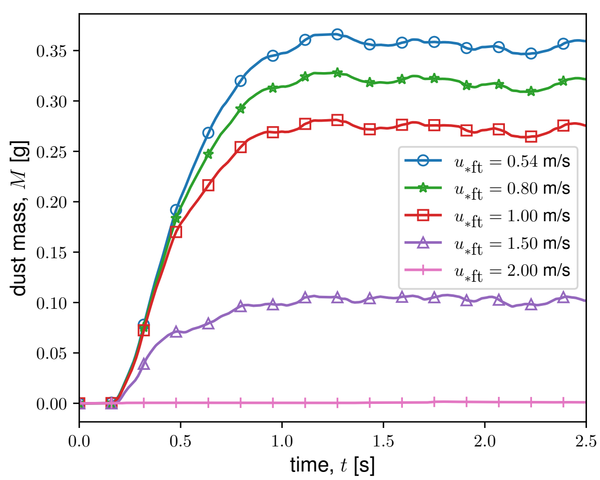

Fig. 16 Computed mass of mobilized dust as a function of time for various fluid threshold velocities.

However, if either of these parameters can be estimated separately within a certain degree of accuracy, the CFD results on dust mass could help reduce the uncertainty on the other. In fact, an independent method to estimate the threshold velocity was used by Lemmon et al. The saltation flow threshold velocity was determined empirically from visual inspection of the video footage by noting the time when the cloud of dust started forming during landing sequences. Knowing the height of the rotorcraft at that time, u_{*ft} was determined as the friction velocity calculated with Rabinovitch et al.'s original model at the corresponding altitude. The advantage of this approach is that it is completely independent of any assumption on the soil properties. The accuracy of the so-estimated u_{*ft} mainly depends on the accuracy of the friction velocity model. On that note, the results presented in Section V.B suggest that the original model may have led to underestimated threshold velocities. If the estimation of u_{*ft} from the video footage was repeated using the modified model instead, the threshold velocity would rather lie between 1.5 to 2.0 $\mathrm{m\,s^{-1}}$, that is, slightly outside of the uncertainty range established by Lemmon et al.

Several sources in the literature report that the threshold velocity for a particle size of $d = 1.4$ µm (assumed here and by Lemmon et al.) is indeed higher than 0.54 $\mathrm{m\,s^{-1}}$ by up to one order of magnitude (see [66, Fig.21(b)]). A threshold velocity of $u_{*ft} \approx 1.5\ \mathrm{m\,s^{-1}}$ could mean that the observed lifted particles were of a size 10 to 50 times bigger. Nevertheless, the outputs of existing models to calculate the threshold velocity of particles as a function of their size also range at least one order of magnitude. Even if the threshold velocity was determined very accurately from the empirical data (assuming there is no error in the friction velocity model), the size of the lifted particles could not be determined with certainty. Additionally, it is still unclear at this stage whether determining u_{*ft} as described here based on a model of the peak average friction velocity is appropriate, considering the highly unsteady character of the velocity in the rotor-induced wall jet.

To conclude, it is desirable to further consolidate the estimation of the friction and threshold velocities as the CFD results could then help reduce the uncertainty on the sandblasting efficiency. Such an insight could help deduce useful information about the soil properties at the location where the rotorcraft operates.

C. Effect of Height

The sensitivity of the amount of dust lifted in the computational domain is assessed with respect to changes in rotorcraft heights for a given threshold velocity of $u_{*ft} = 0.54\ \mathrm{m\,s^{-1}}$. From the implemented dust lifting model, we expect it to primarily depend on the value of u_* through the definition of Q (Eq. (4)), and the ground area where the saltation criterion $u_* > u_{*ft}$ is satisfied.

Figure 17 shows the mass of dust lifted in the simulation as a function of time for Ingenuity hovering at two different heights. On the one hand, the initial increase in dust mass has a very similar slope for both heights. This is another indication that the starting vortex structure drives the initial rate of dust production during the transient, considering that it has a similar circulation and structure in both cases.

On the other hand, the mass of mobilized dust in the established regime exhibits a sensitivity to rotor height, as expected. In this configuration, the simulations reveal that the peak mean u_* drops by approximately 5% between $h/R = 2$ and 4. This corresponds to a change in the average Q of −15%, everything else being kept constant. Yet, the

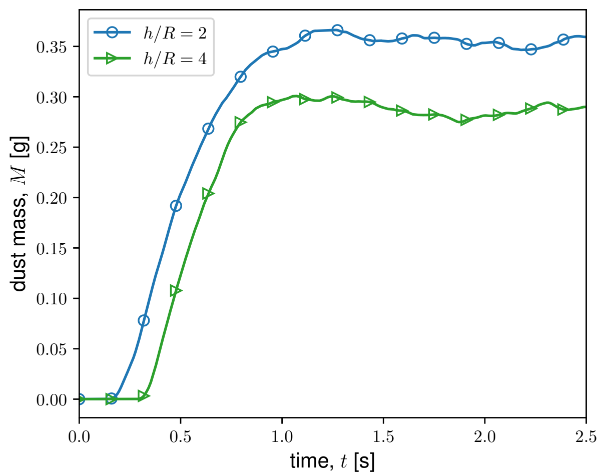

Fig. 17 Computed mass of mobilized dust as a function of time for various rotorcraft heights.

mass of mobilized dust decreases by more than 22%, based on the average of the values presented in Fig. 17 over the last 1.5 s. The difference is due to the area where the saltation criterion is met, which decreases when the hover height increases.

Although these numbers need to be consolidated, the simulations indicate that the mass of mobilized dust is not simply proportional to a characteristic Q based on the the peak mean u_*. In addition to the exposed area, it is also possible that the degree of coherence of the vortical structures that reach the ground vicinity affects the efficiency of the dust-lifting mechanism. As an indicator, Fig. 18 shows the instantaneous friction velocity on the ground surface. When Ingenuity hovers at a height of $h/R = 1$, large regions of high friction velocities are observed. These areas shrink at $h/R = 2$, but they remain shaped as concentric circles, denoting the structure of the coherent vortices. At even larger heights, the areas start to break up in smaller patches, potentially due to more pronounced vortex interactions which are known to render the wake aperiodic [19]. Finer simulations that can more accurately capture the flow features close to the ground are needed to examine how flow coherence affects the dust production mechanisms.

VII. Discussion

Many assumptions have been made in the simulation and modeling framework presented here, as well as in the image processing by Lemmon et al. This limits the representativeness of both datasets compared to the reality on Mars, as well as the scope of the comparison that can be made between them.

Among assumptions that are common between observations and simulations but differ from the actual Martian environment, the particulate matter was assumed to be monodisperse from a single homogeneous species. In reality, dust and sand are better represented with distributions of size and shape. Unfortunately, these distributions are rarely known with certainty, except in a controlled laboratory environment. For the Ingenuity data at hand, virtually all environmental

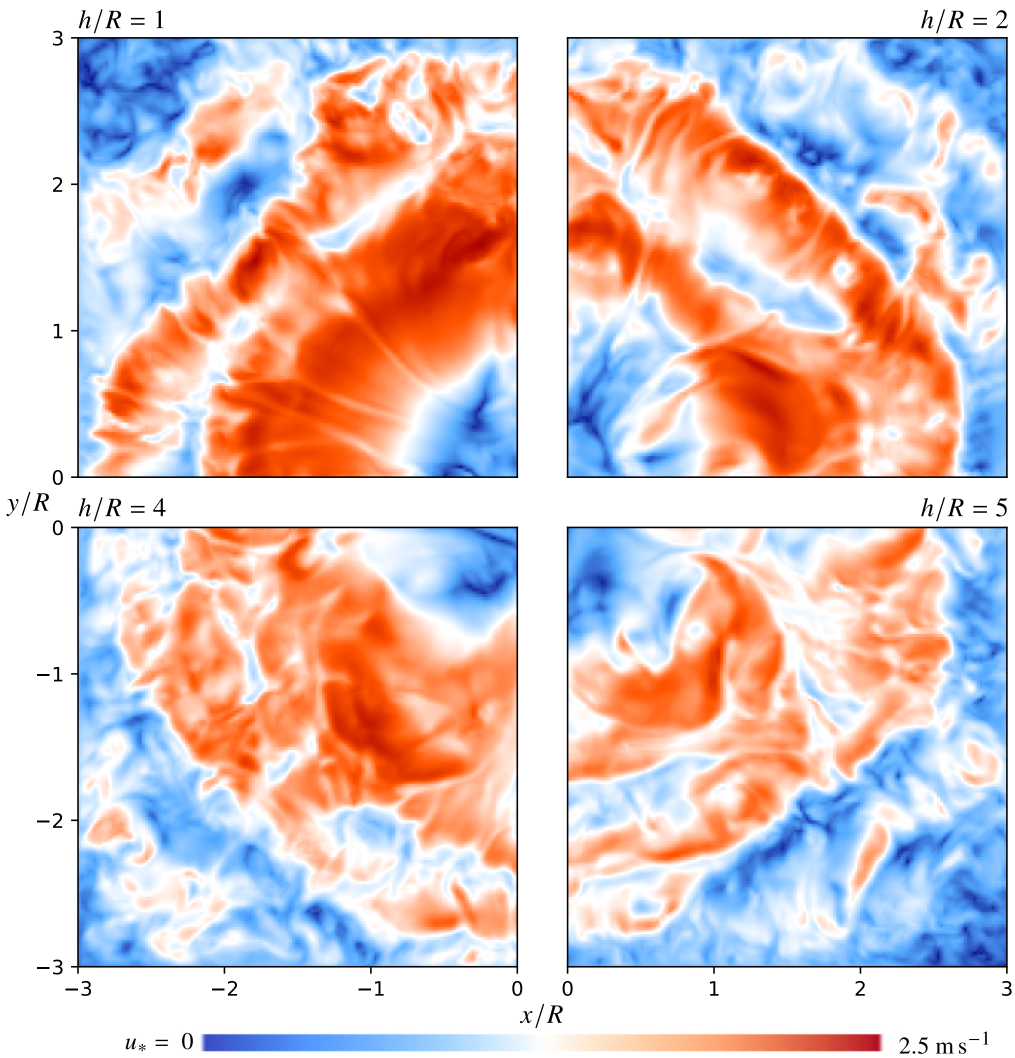

Fig. 18 Instantaneous snapshots of the friction velocity on the ground surface for Ingenuity hovering at various heights.

factors present uncertainty: wind conditions, density of either the solid particles or the atmosphere, soil properties, wall roughness, etc. Additionally, the observational values of the dust mass were obtained through image processing, which introduces additional hypotheses and constraints.

On the simulation side, one of the strongest assumptions made was to neglect the rotorcraft dynamics. Lemmon et al. mention thrust excursions of more than 20% compared to the nominal value that was necessary to execute commands or adjust to gusts. This should be accounted for to improve the consistency between the CFD and the observations. However, the data on the rotorcraft position, acceleration, and control inputs is currently not publicly available. In any case, the calculated mass of dust was limited by the size of the computational domain, which remains smaller than the field of view of the camera in the observations.

As in previous Eulerian brownout simulations of the literature, our model assumed saltation bombardment to be the principal mechanism acting to lift dust in the atmosphere. Although our simulations proved capable of reproducing the phenomenology of the saltation bombardment and vortex-induced trapping, pressure effects and reingestion bombardment were neglected. As highlighted by Lemmon et al. and others, direct aerodynamic lifting of particles or other processes associated with aggregates likely play a role at Mars. These factors limit the accuracy of our simulations. Furthermore, significant uncertainty comes from the saltation and sandblasting models that we used. In particular, the relevance of the concept of sandblasting efficiency is debatable considering the relatively poor predictive performance of existing models, when compared to experimental measurements in various conditions [64, 92]. Even more fundamentally, most aeolian models rely on assumptions which imply the existence of an established turbulent boundary layer flow. As noted by others [33], the rotorwash is home to vortical structures causing shear stress and pressure fluctuations that differ from a regular boundary layer. Our simulation further highlighted the unexpected skewness of the wall shear stress distribution, which questions the applicability of threshold friction velocities and aeolian fluxes derived from regular boundary layer flows. These inconsitencies highlight the need for brownout-dedicated sedimentation parameterizations and their validation, in order to guarantee the accuracy of complete rotorcraft brownout studies. Such parameterizations would ideally account for a large set of environmental properties that are already recognized as influential in the dust emission process (soil properties, size distribution, moisture, atmospheric properties, gravity, etc.) plus flow properties including the unsteadiness associated with large coherent vortical structures. Steps have been taken in this direction using observational data, e.g. in [37, 46, 96], but progress is difficult due to the large number of parameters that need to be controlled. In that respect, Lagrangian simulations such as those presented in [29, 95, 97] have a great potential to help develop process understanding, and extend experimental databases. Despite their relatively high computational cost which limits their application to simplified setups, Lagrangian simulations can directly account for particle-to-particle forces and particle-to-surface cohesion, and therefore explicitly capture vortical flow-driven bombardment or the influence of external pressure forces. Finally, machine learning could prove useful in extracting features and trends from these simulations in order to develop models applicable in a Eulerian context, as proposed by Hardy et al. [98] in a similar context. Until more accurate parameterizations are available, existing models can still be used to perform qualitative assessments of the sensitivity of brownout severity to a rotorcraft geometry [99]. We envision that such approach could be leveraged in preparation of future planetary rotorcraft designs.

Among other parameters affecting the accuracy of the numerical models, the effect of the impact threshold velocity should be evaluated. Additionally, preliminary tests showed that the turbulent Schmidt number can significantly affect the calculated mass of mobilized dust. However, we could not find a readily available value in the literature for such a parameter. Let us also note that the accuracy of the friction velocity obtained from the CFD is contingent upon the capacity of the simulation to resolve the flow in the vicinity of the wall. In the present work, the simulation relied on a simplified representation of the wall that has shown favorable agreement with numerical and experimental velocity profiles in the outwash of a rotorcraft. Still, before drawing any definitive conclusion, we recommend that the results presented here be consolidated by comparison with other numerical methods' predictions based on properly wall-resolved or wall-modeled schemes.

From an engineering perspective, it could be useful to derive a model of the dust production based on a statistical representation of the friction velocity and the related saltation fluxes. To this end, we have suggested using the peak average u_* and a high likely percentile value, although it is unclear whether these two indicators are sufficient to represent a quantity that is inherently stochastic. The results of this work also underlined that dust production depends on a characteristic area where the saltation threshold is exceeded. Ideally, this information should be incorporated in a predictive model. Additional efforts are needed to derive and validate refined engineering models.

Finally, when it comes to comparing numerical and observational data, it should be mentioned that take-off and landing phases are quite different. The results from one should not be interchangeably used with the other. During take-off, the amount of lifted dust primarily depends on the development of the starting vortex, which is associated with higher circulation and induced velocity. This potent structure is similar to the ground horseshoe vortex forming when the rotor translates laterally at low speeds, which was shown to drive dust emission at low advance ratios [21, 31, 33]. On the other hand, landing conditions are closer to established hover if the rotorcraft approaches the ground slowly. In Section V, the initial transient was explicitly removed from the simulation results in order to focus on the established regime. On the other hand, the comparison presented in Section VI focused exclusively on the transient phase because the amount of dust tracked in the simulation and visible in the observation are compatible only during the first instants of the flight. Nevertheless, there is an opportunity to extend the comparisons to the landing phase, although this would require larger computational domains in order to cover a wider area and track a more significant amount of dust.

VIII. Conclusions

The objectives of this research were to showcase the efficacy of modern numerical models to simulate brownout on other planets by comparison with Lemmon et al.'s dataset. Despite the undeniably strong assumptions made in the simulation model as well as in the observational data processing, we reach the following conclusions:

- Critical environmental parameters driving the amount of dust lifted up during the simulation have been identified: the friction velocity at the wall, the saltation threshold velocities ($u_{*\mathrm{it}}$, $u_{*\mathrm{ft}}$), and the sandblasting efficiency.
- Among these, numerical simulations are most valuable in reducing the uncertainty on the friction velocity. Distributions of u_* in the rotorwash have been calculated at several radial locations and for various rotor heights. Although such statistical representation is oblivious to the presence of coherent vortical structures, the distributions skewness is atypical of regular turbulent boundary layers, denoting the particular flow conditions of the wall jet.
- The simulation results suggested that the sensitivity of the friction velocity to the height of the rotorcraft may have been overestimated in existing analytical models (Fig. 13). A modified model of the peak mean u_* has been presented, together with a a fit of the peak 99.5^{th} percentile of the friction velocity distribution. These expressions

are valid for a rotor hovering at a height between one and six rotor radii.

- When comparing the calculated and the empirically-derived mass of mobilized dust, it is virtually impossible to discriminate the effect of the saltation threshold velocity versus the sandblasting efficiency. Both parameters depend on soil properties that are not easily determined or measured. Additionally, they suffer from modeling uncertainty that leads to orders of magnitude variations of the computed mass of dust. However, reducing the uncertainty in either of the parameters could help provide insights on the other. This could be achieved through dedicated measurements, or Lagrangian simulations with an explicit treatment of the forces acting on each particle, including lift, drag, interparticle cohesion, and gravity contributions.
- For a set of arbitrarily chosen environmental parameters, the results from the simulations emulating take-off suggested that the rate of production of mobilized dust primarily depends on the development of the starting vortex emanating from the impulsively started rotors. In the established regime, the numerical results corroborated that the mass of mobilized dust does not only depend on the flux of dust at the wall based on some characteristic friction velocity. The area where the saltation criterion is exceeded also plays a role, as may other details of the local vortex dynamics.

Although its usability is hampered by inherent uncertainty, the data derived from Ingenuity's observations provided a wealth of information that still has secrets to unveil. Beyond that, Ingenuity's unprecedented achievements certainly paved the way for future exploration missions on extraterrestrial worlds.

IX. Appendix

The PDFs shown in Fig. 12 are constructed from the statistics of the friction velocity collected at various radial locations as a function of time and azimuth. These PDFs can be fitted with a skewed normal distribution

$$f_X(x) = \frac{1}{\omega\pi} e^{-\frac{(x-\xi)^2}{2\omega^2}} \int_{-\infty}^{\alpha\left(\frac{x-\xi}{\omega}\right)} e^{-\frac{t^2}{2}}\, \mathrm{d}t, \tag{15}$$

with ξ the location parameter, ω the scale parameter, and α the skewness.

Figure 19 shows the result of curve fitting of the histograms constructed from the statistics. A fair agreement is observed between the curves for all locations $r/R \geq 1$. The procedure is repeated for several rotor heights. Table 4 presents the parameters of the fitted distributions. When the wall jet is established, the skewness seems to be roughly independent from the radial location and approximately equal to -2. It takes a longer radial distance for the wall jet to establish when the rotor height increases.

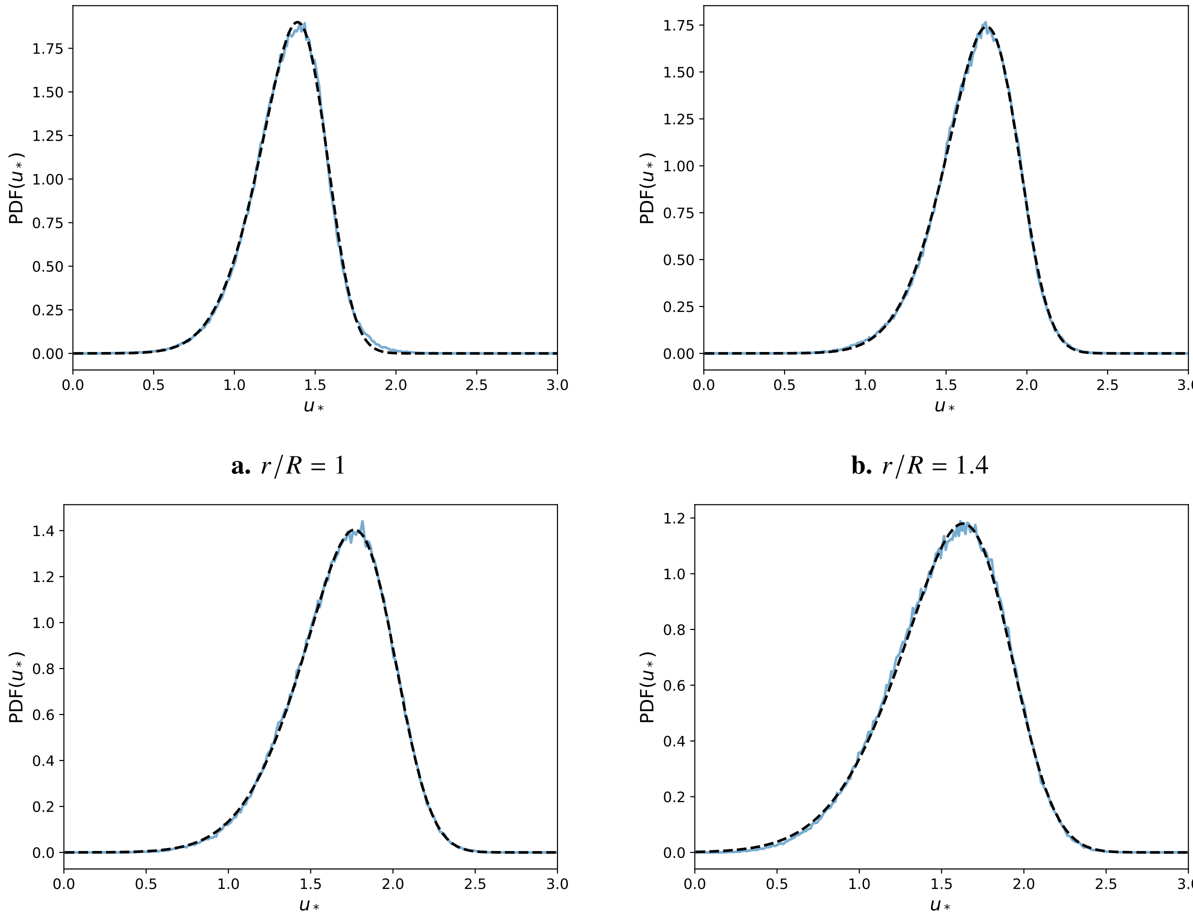

a. $r/R = 1$ **b.** $r/R = 1.4$

c. $r/R = 1.8$ **d.** $r/R = 2.2$

Fig. 19 Fit of the observed friction velocity histogram (blue solid) with a skewed normal PDF (black dashed) at various radial locations for Ingenuity hovering at $h/R = 2$.

X. Acknowledgments

D.-G. Caprace is supported by an appointment to the NASA Postdoctoral Program at the NASA Ames Research Center, administered by Oak Ridge Associated Universities under contract with NASA. P. Ventura Diaz is supported by the Revolutionary Vertical Lift Technology (RVLT) Project. Resources supporting this work were provided by the NASA High-End Computing (HEC) Program through the NASA Advanced Supercomputing (NAS) Division at NASA Ames Research Center. The authors express their deep gratitude to Profs. Philippe Chatelain and Grégoire Winckelmans (UCLouvain, Belgium) for providing access to the source code of VPM4x.

Table 4 Parameters of the fitted distributions at various radial locations for Ingenuity hovering at different heights: location ξ, scale ω, skewness α, mean μ, standard deviation σ.

h/R	r/R	ξ	ω	α	μ	σ
2	1.0	1.56	0.32	−2.14	1.33	0.22
	1.4	1.93	0.34	−2.06	1.69	0.24
	1.8	1.99	0.43	−2.21	1.68	0.30
	2.2	1.89	0.51	−2.17	1.53	0.35
3	1.0	1.58	0.31	−1.77	1.34	0.22
	1.4	1.92	0.34	−2.24	1.67	0.24
	1.8	1.92	0.37	−2.05	1.66	0.26
	2.2	1.86	0.46	−2.51	1.52	0.31
4	1.0	1.52	0.27	−1.27	1.35	0.21
	1.4	1.83	0.30	−1.64	1.62	0.22
	1.8	1.83	0.33	−1.65	1.60	0.24
	2.2	1.76	0.39	−2.04	1.48	0.27
5	1.0	1.44	0.24	−1.03	1.31	0.20
	1.4	1.72	0.27	−1.18	1.55	0.22
	1.8	1.73	0.31	−1.32	1.53	0.24
	2.2	1.68	0.38	−1.81	1.42	0.27

References

[1] Young, L. A., Chen, R. T., Aiken, E. W., and Briggs, G. A., "Design opportunities and challenges in the development of vertical lift planetary aerial vehicles," *American Helicopter Society (AHS) Vertical Lift Aircraft Design Conference*, San Francisco, CA, 2000.

[2] Dull, C., Wagner, L., Young, L., and Johnson, W., "Hover and forward flight performance modeling of the Ingenuity Mars Helicopter," *Aeromechanics for Advanced Vertical Flight Technical Meeting, Transformative Vertical Flight*, edited by American Helicopter Society, San Jose, CA, 2022.

[3] Tzanetos, T., Aung, M., Balaram, J., Grip, H. F., Karras, J. T., Canham, T. K., Kubiak, G., Anderson, J., Merewether, G., Starch, M., Pauken, M., Cappucci, S., Chase, M., Golombek, M., Toupet, O., Smart, M. C., Dawson, S., Ramirez, E. B., Lam, J., Stern, R., Chahat, N., Ravich, J., Hogg, R., Pipenberg, B., Keennon, M., and Williford, K. H., "Ingenuity Mars Helicopter: From Technology Demonstration to Extraterrestrial Scout," *2022 IEEE Aerospace Conference (AERO)*, 2022, pp. 01–19. https://doi.org/10.1109/AERO53065.2022.9843428.

[4] Grip, H. F., Johnson, W., Malpica, C., Scharf, D. P., Mandić, M., Young, L., Allan, B., Mettler, B., Martin, M. S., and Lam, J., "Modeling and Identification of Hover Flight Dynamics for NASA's Mars Helicopter," *Journal of Guidance, Control, and Dynamics*, Vol. 43, No. 2, 2020, pp. 179–194. https://doi.org/10.2514/1.G004228, URL https://doi.org/10.2514/1.G004228.

[5] Tzanetos, T., Bapst, J., Kubiak, G., Tosi, L. P., Sirlin, S., Brockers, R., Delaune, J., Grip, H. F., Matthies, L., Balaram, J., Withrow-Maser, S., Johnson, W., Young, L., and Pipenberg, B., "Future of Mars Rotorcraft - Mars Science Helicopter," *2022 IEEE Aerospace Conference (AERO)*, 2022, pp. 1–16. https://doi.org/10.1109/AERO53065.2022.9843501.

[6] Lorenz, R. D., *Planetary Exploration with Dragonfly and Ingenuity*, American Institute of Aeronautics and Astronautics, Inc., 2022. https://doi.org/10.2514/4.106378.

[7] Leishman, J., et al., "Rotorcraft Brownout Advanced Understanding, Control, and Mitigation," *Final Report, FA9550-08-1-0406*, 2014.

[8] Grip, H. F., Conway, D., Lam, J., Williams, N., Golombek, M. P., Brockers, R., Mischna, M., and Cacan, M. R., "Flying a Helicopter on Mars: How Ingenuity's Flights were Planned, Executed, and Analyzed," *2022 IEEE Aerospace Conference (AERO)*, 2022, pp. 1–17. https://doi.org/10.1109/AERO53065.2022.9843813.

[9] Young, L., Aiken, E., Lee, P., and Briggs, G., "Mars rotorcraft: possibilities, limitations, and implications for human/robotic exploration," *2005 IEEE Aerospace Conference*, 2005, pp. 300–318. https://doi.org/10.1109/AERO.2005.1559324.

[10] Young, L. A., Delaune, J., Johnson, W., Withrow, S., Cummings, H., Sklyanskiy, E., Izraelevitz, J., Schutte, A., Fraeman, A., and Bhagwat, R., "Design Considerations for a Mars Highland Helicopter," *ASCEND 2020*, virtual, 2020. https://doi.org/10.2514/6.2020-4027, URL https://arc.aiaa.org/doi/abs/10.2514/6.2020-4027.

[11] Rutter, C., and Lach, M., "Feasibility Study of a Robotic Science Arm on Future Martian Rotorcraft," *Aeromechanics for Advanced Vertical Flight Technical Meeting, Transformative Vertical Flight*, edited by American Helicopter Society, San Jose, CA, 2022.

[12] Anderson, J. L., Karras, J. T., Cacan, M., Kubiak, G., Pyrzak, G., Dor, H., and Pipenberg, B., "Ingenuity, One Year of Flying on Mars," *IEEE Aerospace Conference*, 2023, pp. 1–18. https://doi.org/10.1109/AERO55745.2023.10115837.

[13] Lorenz, R. D., "Triboelectric Charging and Brownout Hazard Evaluation for a Planetary Rotorcraft," *AIAA AVIATION 2020 FORUM*, 2020. https://doi.org/10.2514/6.2020-2837.

[14] Rabinovitch, J., Lorenz, R., Slimko, E., and Wang, K.-S. C., "Scaling sediment mobilization beneath rotorcraft for Titan and Mars," *Aeolian Research*, Vol. 48, 2021, p. 100653. https://doi.org/10.1016/j.aeolia.2020.100653.

[15] Lorenz, R. D., "Sand Transport on Titan: A Sticky Problem," *Geophysical Research Letters*, Vol. 49, No. 10, 2022, p. e2022GL098375. https://doi.org/10.1029/2022GL098375.

[16] Shao, Y., *Physics and Modelling of Wind Erosion*, Springer Netherlands, Dordrecht, 2008. https://doi.org/10.1007/978-1-4020-8895-7_9, URL https://doi.org/10.1007/978-1-4020-8895-7_9.

[17] Shao, Y., Raupach, M. R., and Findlater, P. A., "Effect of saltation bombardment on the entrainment of dust by wind," *Journal of Geophysical Research: Atmospheres*, Vol. 98, No. D7, 1993, pp. 12719–12726. https://doi.org/https://doi.org/10.1029/93JD00396, URL https://agupubs.onlinelibrary.wiley.com/doi/abs/10.1029/93JD00396.

[18] Lu, H., and Shao, Y., "A new model for dust emission by saltation bombardment," *Journal of Geophysical Research: Atmospheres*, Vol. 104, No. D14, 1999, pp. 16827–16842. https://doi.org/https://doi.org/10.1029/1999JD900169, URL https://agupubs.onlinelibrary.wiley.com/doi/abs/10.1029/1999JD900169.

[19] Johnson, B., Leishman, J. G., and Sydney, A., "Investigation of Sediment Entrainment Using DualPhase, HighSpeed Particle Image Velocimetry," *Journal of the American Helicopter Society*, Vol. 55, No. 4, 2010, p. 42003. https://doi.org/doi:10.4050/JAHS.55.042003, URL https://www.ingentaconnect.com/content/ahs/jahs/2010/00000055/00000004/art00003.

[20] Sydney, A., and Leishman, J. G., "Time-resolved measurements of rotor-induced particle flows produced by a hovering rotor," *Journal of the American Helicopter Society*, Vol. 59, No. 2, 2014, pp. 1–16.

[21] Nathan, N., and Green, R., "Measurements of a rotor flow in ground effect and visualization of the brown-out phenomenon," *Aeronautical Journal*, Vol. 113, No. 1145, 2008, pp. 467–478.

[22] Sydney, A., Baharani, A., and Leishman, J., "Understanding brownout using near-wall dual-phase flow measurements," *67th Annual Forum Proceedings of the American Helicopter Society, Virginia Beach, VA*, 2011.

[23] Rauleder, J., and Leishman, J. G., "Particle–fluid interactions in rotor-generated vortex flows," *Experiments in Fluids*, Vol. 55, No. 3, 2014, p. 1689. https://doi.org/10.1007/s00348-014-1689-5, URL https://doi.org/10.1007/s00348-014-1689-5.

[24] Wadcock, A. J., Ewing, L. A., Solis, E., Potsdam, M., and Rajagopalan, G., "Rotorcraft downwash flow field study to understand the aerodynamics of helicopter brownout," *AHS Southwest Region Technical Specialist"s Meeting" Technologies for Next Generation of Vertical Life Aircraft"*, 2008.

[25] Rauleder, J., and Leishman, J. G., "Flow Environment and Organized Turbulence Structures Near a Plane Below a Rotor," *AIAA Journal*, Vol. 52, No. 1, 2014, pp. 146–161. https://doi.org/10.2514/1.J052315, URL https://doi.org/10.2514/1.J052315.

[26] Phillips, C., and Brown, R. E., "Eulerian Simulation of the Fluid Dynamics of Helicopter Brownout," *Journal of Aircraft*, Vol. 46, No. 4, 2009, pp. 1416–1429. https://doi.org/10.2514/1.41999.

[27] Jiang, X., Xu, Y., Geng, Y., Meng, L., Ahmed, M., Wang, C., and Lu, H., "Modeling of air and particles flow with revolving rotor hovering over the particles layer," *Powder Technology*, Vol. 376, 2020, pp. 272–284. https://doi.org/https://doi.org/10.1016/j.powtec.2020.07.113, URL https://www.sciencedirect.com/science/article/pii/S0032591020307373.

[28] Phillips, C., Kim, H. W., and Brown, R. E., "Helicopter brownout – Can it be modelled?" *The Aeronautical Journal*, Vol. 115, No. 1164, 2011, pp. 123–133. https://doi.org/10.1017/S0001924000005510.

[29] Morales, F., and Squires, K., "Simulation of Rotor Vortex Interactions with a Particle-Laden Turbulent Boundary Layer," *6th AIAA Theoretical Fluid Mechanics Conference*, 2011. https://doi.org/10.2514/6.2011-4041, URL https://arc.aiaa.org/doi/abs/10.2514/6.2011-4041.

[30] Cao, Y., Wang, G., and Jiang, C., "Study on Influencing Factors of Helicopter Brownout Evolution Based on CFD-DEM," *Applied Sciences*, Vol. 12, No. 1, 2022. https://doi.org/10.3390/app12010126, URL https://www.mdpi.com/2076-3417/12/1/126.

[31] Lin, H., Xu, C., Jiang, C., Hu, S., and Lee, C.-H., "Finite Particle Approach for High-Fidelity Simulation on Helicopter Brownout," *AIAA Journal*, Vol. 62, No. 1, 2024, pp. 193–208. https://doi.org/10.2514/1.J063230, URL https://doi.org/10.2514/1.J063230.

[32] Wachspress, D., Whitehouse, G., Keller, J. D., Yu, K., Gilmore, P., Dorsett, M., and McClure, K., “A high fidelity brownout model for real-time flight simulations and trainers,” *Proceedings of the 65th Annual American Helicopter Society Forum*, 2009.

[33] Syal, M., and Leishman, J. G., “Modeling of Bombardment Ejections in the Rotorcraft Brownout Problem,” *AIAA Journal*, Vol. 51, No. 4, 2013, pp. 849–866. https://doi.org/10.2514/1.J051761, URL https://doi.org/10.2514/1.J051761.

[34] Rovere, F., Barakos, G. N., and Steijl, R., “Comparison between Eulerian and Lagrangian methods to predict brownout clouds,” *Aerospace Science and Technology*, Vol. 137, 2023, p. 108306. https://doi.org/10.1016/j.ast.2023.108306.

[35] Syal, M., Govindarajan, B., and Leishman, J., “Mesoscale sediment tracking methodology to analyze brownout cloud developments,” *Proceedings of the American Helicopter Society, 66th Annual Forum*, Vol. 1, 2010, p. 3.

[36] Govindarajan, B., Leishman, J. G., and Gumerov, N. A., “Particle-Clustering Algorithms for the Prediction of Brownout Dust Clouds,” *AIAA Journal*, Vol. 51, No. 5, 2013, pp. 1080–1094. https://doi.org/10.2514/1.J051907, URL https://doi.org/10.2514/1.J051907.

[37] Cowherd, C., “Sandblaster 2 support of see-through technologies for particulate brownout: Task 5 Technical Report,” *Defense Advanced Research Projects Agency (DOD) Strategic Technology Office, Tech. Rept. MRI Project*, , No. 110565, 2007.

[38] Milluzzo, J., and Leishman, J. G., “Assessment of rotorcraft brownout severity in terms of rotor design parameters,” *Journal of the American Helicopter Society*, Vol. 55, No. 3, 2010, pp. 32009–32009.

[39] Gillies, J., Etyemezian, V., Kuhns, H., McAlpine, J., King, J., Uppapalli, S., Nikolich, G., and Engelbrecht, J., “Dust emissions created by low-level rotary-winged aircraft flight over desert surfaces,” *Atmospheric Environment*, Vol. 44, No. 8, 2010, pp. 1043–1053. https://doi.org/https://doi.org/10.1016/j.atmosenv.2009.12.018, URL https://www.sciencedirect.com/science/article/pii/S1352231009010528.

[40] Rodgers, S. J., *Evaluation of the dust cloud generated by helicopter rotor downwash*, US Army Aviation Materiel Laboratories, 1968.

[41] Wong, O. D., and Tanner, P. E., “Photogrammetric Measurements of an EH-60L Brownout Cloud,” *Journal of the American Helicopter Society*, Vol. 61, No. 1, 2016, pp. 1–10. https://doi.org/10.4050/JAHS.61.012003, URL https://www.ingentaconnect.com/content/ahs/jahs/2016/00000061/00000001/art00004.

[42] Tritschler, J., and Celi, R., “Brownout Cloud Characterization Using the Modulation Transfer Function,” *Journal of the American Helicopter Society*, Vol. 58, No. 1, 2013, pp. 1–13.

[43] Tan, J. F., Ge, Y. Y., Zhang, W. G., Cui, Z., and Wang, H. W., “Numerical study on helicopter brownout with crosswind,” *Aerospace Science and Technology*, Vol. 131, 2022, p. 107965. https://doi.org/https://doi.org/10.1016/j.ast.2022.107965, URL https://www.sciencedirect.com/science/article/pii/S1270963822006393.

[44] Thomas, S., Lakshminarayan, V. K., Kalra, T. S., and Baeder, J. D., "Eulerian-Lagrangian analysis of cloud evolution using CFD coupled with a sediment tracking algorithm," *67th Annual Forum of the American Helicopter Society*, edited by American Helicopter Society, Virginia Beach, VA, 2011.

[45] Syal, M., and Leishman, J. G., "Predictions of Brownout Dust Clouds Compared to Photogrammetry Measurements," *Journal of the American Helicopter Society*, Vol. 58, No. 2, 2013, pp. 1–18. https://doi.org/doi:10.4050/JAHS.58.022001, URL https://www.ingentaconnect.com/content/ahs/jahs/2013/00000058/00000002/art00001.

[46] Perrotta, G., Glucksman-Glaser, M., and Jones, A. R., "Similarity Parameters for the Characterization of Sediment Mobilization by Unsteady Rotor Wakes," *Journal of Aircraft*, Vol. 52, No. 6, 2015, pp. 2090–2095. https://doi.org/10.2514/1.C033245, URL https://doi.org/10.2514/1.C033245.

[47] Lemmon, M. T., Lorenz, R. D., Rabinovitch, J., Newman, C. E., Williams, N. R., Sullivan, R., Golombek, M. P., Bell III, J. F., Maki, J. N., and Vicente-Retortillo, A., "Lifting and Transport of Martian Dust by the Ingenuity Helicopter Rotor Downwash as Observed by High-Speed Imaging From the Perseverance Rover," *Journal of Geophysical Research: Planets*, Vol. 127, No. 12, 2022, p. e2022JE007605. https://doi.org/10.1029/2022JE007605.

[48] Lorenz, R. D., "Gentle Perseverance Lifts the Veil on Martian Dust," *Journal of Geophysical Research: Planets*, Vol. 128, No. 9, 2023, p. e2023JE007843. https://doi.org/https://doi.org/10.1029/2023JE007843, URL https://agupubs.onlinelibrary.wiley.com/doi/abs/10.1029/2023JE007843, e2023JE007843 2023JE007843.

[49] Winckelmans, G., Cocle, R., Dufresne, L., and Capart, R., "Vortex methods and their application to trailing wake vortex simulations," *C. R. Phys.*, Vol. 6, No. 4-5, 2005, pp. 467–486. https://doi.org/10.1016/j.crhy.2005.05.001.

[50] Chatelain, P., Curioni, A., Bergdorf, M., Rossinelli, D., Andreoni, W., and Koumoutsakos, P., "Billion vortex particle Direct Numerical Simulations of aircraft wakes," *Computer Methods in Applied Mechanics and Engineering*, Vol. 197, No. 13, 2008, pp. 1296–1304. https://doi.org/10.1016/j.cma.2007.11.016.

[51] Caprace, D.-G., Winckelmans, G., and Chatelain, P., "An immersed lifting and dragging line model for the vortex particle-mesh method," *Theoretical and Computational Fluid Dynamics*, Vol. 34, 2020, pp. 21–48. https://doi.org/10.1007/s00162-019-00510-1.

[52] Mimeau, C., and Mortazavi, I., "A Review of Vortex Methods and Their Applications: From Creation to Recent Advances," *Fluids*, Vol. 6, No. 2, 2021. https://doi.org/10.3390/fluids6020068, URL https://www.mdpi.com/2311-5521/6/2/68.

[53] Jeanmart, H., and Winckelmans, G., "Investigation of eddy-viscosity models modified using discrete filters: A simplified regularized variational multiscale model and an enhanced field model," *Physics of Fluids*, Vol. 19, No. 5, 2007, p. 055110. https://doi.org/10.1063/1.2728935.

[54] Caprace, D.-G., Chatelain, P., and Winckelmans, G., "Wakes of rotorcraft in advancing flight: A large eddy simulation study," *Physics of Fluids*, Vol. 32, No. 8, 2020, p. 087107. https://doi.org/10.1063/5.0015162.

[55] Caprace, D.-G., Winckelmans, G., and Chatelain, P., “Assessment of the Vortex Particle-Mesh Method for Efficient LES of Hovering Rotors and their Wakes,” *AIAA Scitech 2021 Forum*, 2021. https://doi.org/10.2514/6.2021-0738.

[56] Caprace, D.-G., Ning, A., Chatelain, P., and Winckelmans, G., “Effects of rotor-airframe interaction on the aeromechanics and wake of a quadcopter in forward flight,” *Aerospace Science and Technology*, 2022, p. 107899. https://doi.org/10.1016/j.ast.2022.107899, URL https://www.sciencedirect.com/science/article/pii/S1270963822005739.

[57] Caprace, D.-G., and Ning, A., “Large Eddy Simulation for Empirical Modeling of the Wake of Three Urban Air Mobility Vehicles,” *Journal of the American Helicopter Society*, Vol. 64, No. 4, 2023, pp. pp. 42002–42017(16). https://doi.org/10.4050/JAHS.68.042002.

[58] Caprace, D.-G., Diaz, P. V., and Yoon, S., “Simulation of a Single Rotor and a Quadrotor Hovering in Full and Partial Ground Effect,” *AIAA AVIATION 2023 Forum*, San Diego, CA, 2023. https://doi.org/10.2514/6.2023-4281, URL https://arc.aiaa.org/doi/abs/10.2514/6.2023-4281.

[59] Caprace, D.-G., Ventura Diaz, P., and Yoon, S., “Simulation of the Rotorwash Induced by a Quadrotor Urban Air Taxi in Ground Effect,” *79th VFS annual forum*, edited by V. F. Society, West Palm Beach, Florida, 2023.

[60] Reichardt, H., “Vollständige Darstellung der turbulenten Geschwindigkeitsverteilung in glatten Leitungen,” *ZAMM - Journal of Applied Mathematics and Mechanics / Zeitschrift für Angewandte Mathematik und Mechanik*, Vol. 31, No. 7, 1951, pp. 208–219. https://doi.org/10.1002/zamm.19510310704.

[61] Koning, W. J., Johnson, W., and Allan, B. G., “Generation of mars helicopter rotor model for comprehensive analyses,” *AHS Specialists’ Conference on Aeromechanics Design for Transformative Vertical Flight*, edited by American Helicopter Society, San Jose, CA, 2018.

[62] Pipenberg, B. T., Keennon, M., Tyler, J., Hibbs, B., Langberg, S., Balaram, J. B., Grip, H. F., and Pempejian, J., “Design and Fabrication of the Mars Helicopter Rotor, Airframe, and Landing Gear Systems,” *AIAA Scitech 2019 Forum*, 2019. https://doi.org/10.2514/6.2019-0620, URL https://arc.aiaa.org/doi/abs/10.2514/6.2019-0620.

[63] Drela, M., “XFOIL: An analysis and design system for low Reynolds number airfoils,” *Low Reynolds number aerodynamics*, Springer, 1989, pp. 1–12. https://doi.org/10.1007/978-3-642-84010-4_1.

[64] Tian, R., Ma, X., and Zhao, J., “A revised mineral dust emission scheme in GEOS-Chem: improvements in dust simulations over China,” *Atmospheric Chemistry and Physics*, Vol. 21, No. 6, 2021, pp. 4319–4337. https://doi.org/10.5194/acp-21-4319-2021, URL https://acp.copernicus.org/articles/21/4319/2021/.

[65] Joshi, J. R., “Dust model sensitivity to dust source mask, sandblasting efficiency, air density, and land use: Implications for model improvement,” *Atmospheric Pollution Research*, Vol. 15, No. 10, 2024, p. 102230. https://doi.org/https://doi.org/10.1016/j.apr.2024.102230, URL https://www.sciencedirect.com/science/article/pii/S1309104224001958.

[66] Kok, J. F., Parteli, E. J. R., Michaels, T. I., and Karam, D. B., "The physics of wind-blown sand and dust," *Reports on Progress in Physics*, Vol. 75, No. 10, 2012, p. 106901. https://doi.org/10.1088/0034-4885/75/10/106901.

[67] Bagnold, R. A., *The physics of blown sand and desert dunes*, Methuen and Co., London, 1941.

[68] Kok, J. F., "An improved parameterization of wind-blown sand flux on Mars that includes the effect of hysteresis," *Geophysical Research Letters*, Vol. 37, No. 12, 2010. https://doi.org/https://doi.org/10.1029/2010GL043646, URL https://agupubs.onlinelibrary.wiley.com/doi/abs/10.1029/2010GL043646.

[69] Kawamura, R., "Study of sand movement by wind," Tech. Rep. Translated (1965) as Report HEL 2–8, University of California Hydraulics Engineering Laboratory, Berkeley, 1951.

[70] White, B. R., "soil transport by winds on Mars," *Journal of Geophysical Research: Solid Earth*, Vol. 84, No. B9, 1979, pp. 4643–4651. https://doi.org/10.1029/JB084iB09p04643.

[71] Alfaro, S. C., Gaudichet, A., Gomes, L., and Maillé, M., "Modeling the size distribution of a soil aerosol produced by sandblasting," *Journal of Geophysical Research: Atmospheres*, Vol. 102, No. D10, 1997, pp. 11239–11249. https://doi.org/https://doi.org/10.1029/97JD00403, URL https://agupubs.onlinelibrary.wiley.com/doi/abs/10.1029/97JD00403.

[72] Zobeck, T. M., "Abrasion of Crusted Soils: Influence of Abrader Flux and Soil Properties," *Soil Science Society of America Journal*, Vol. 55, No. 4, 1991, pp. 1091–1097. https://doi.org/https://doi.org/10.2136/sssaj1991.03615995005500040033x, URL https://acsess.onlinelibrary.wiley.com/doi/abs/10.2136/sssaj1991.03615995005500040033x.

[73] Rice, M. A., Willetts, B. B., and McEwan, I. K., "Observations of collisions of saltating grains with a granular bed from high-speed cine-film," *Sedimentology*, Vol. 43, No. 1, 1996, pp. 21–31. https://doi.org/https://doi.org/10.1111/j.1365-3091.1996.tb01456.x, URL https://onlinelibrary.wiley.com/doi/abs/10.1111/j.1365-3091.1996.tb01456.x.

[74] Gillette, D., "Environmental factors affecting dust emission by wind erosion," *Saharan dust*, 1979, pp. 71–94.

[75] Ramasamy, M., and Yamauchi, G. K., "Using Model-Scale Tandem-Rotor Measurements in Ground Effect to Understand Full-Scale CH-47D Outwash," *Journal of the American Helicopter Society*, Vol. 62, No. 1, 2017, pp. 1–14. https://doi.org/10.4050/JAHS.62.012004.

[76] Silva, M., and Riser, R., "CH-47D tandem rotor outwash survey," *67th Annual Forum of the American Helicopter Society*, edited by American Helicopter Society, Virginia Beach, VA, 2011.

[77] Braukmann, J. N., Schwarz, C., Wolf, C., Buron, E., Koch, S., Buske, G., and Gardner, A., "BOS and Hot-Film Analysis of a CH-53G Helicopter Wake in Ground Effect," *79th Vertical Flight Society Annual Forum and Technology Display*, edited by American Helicopter Society, 2023, pp. 1–15.

[78] Srinivas, A. L., Zhang, J., and Hu, R., "Parametrizing the probability density function of wall-shear stress in turbulent channel flows," *Phys. Rev. Fluids*, Vol. 9, 2024, p. 124604. https://doi.org/10.1103/PhysRevFluids.9.124604, URL https://link.aps.org/doi/10.1103/PhysRevFluids.9.124604.

[79] Wang, J., Pan, C., and Wang, J., "Characteristics of fluctuating wall-shear stress in a turbulent boundary layer at low-to-moderate Reynolds number," *Phys. Rev. Fluids*, Vol. 5, 2020, p. 074605. https://doi.org/10.1103/PhysRevFluids.5.074605, URL https://link.aps.org/doi/10.1103/PhysRevFluids.5.074605.

[80] Ramasamy, M., Heineck, J. T., Yamauchi, G. K., Schairer, E., and Norman, T. R., "Comprehensive Aerodynamic Analysis of PIV Measurements in the NFAC 80- by 120-ft Test Section Towards Understanding HVAB Hovering Rotor Characteristics," *Vertical Flight Society's 80th Annual Forum & Technology Display*, 2024.

[81] Hariharan, N. S., "An Overview of Wake-Breakdown in High-Fidelity Simulations of Rotor in Hover," *AIAA Scitech 2020 Forum*, 2020. https://doi.org/10.2514/6.2020-0530, URL https://arc.aiaa.org/doi/abs/10.2514/6.2020-0530.

[82] Hohler, D., "An analytical method of determining general downwash flow field parameters for VSTOL Aircraft," Tech. rep., Air Force Wright Aeronautical Labs, Wright-Patterson AFB, OH, 1966.

[83] Roney, J. A., and White, B. R., "Estimating fugitive dust emission rates using an environmental boundary layer wind tunnel," *Atmospheric Environment*, Vol. 40, No. 40, 2006, pp. 7668–7685. https://doi.org/https://doi.org/10.1016/j.atmosenv.2006.08.015, URL https://www.sciencedirect.com/science/article/pii/S1352231006008028.

[84] Panebianco, J. E., Mendez, M. J., and Buschiazzo, D. E., "PM10 Emission, Sandblasting Efficiency and Vertical Entrainment During Successive Wind-Erosion Events: A Wind-Tunnel Approach," *Boundary-Layer Meteorology*, Vol. 161, No. 2, 2016, pp. 335–353. https://doi.org/10.1007/s10546-016-0172-7, URL https://doi.org/10.1007/s10546-016-0172-7.

[85] Gelbart, G., and Katra, I., "Dependence of the Dust Emission on the Aggregate Sizes in Loess Soils," *Applied Sciences*, Vol. 10, No. 16, 2020. https://doi.org/10.3390/app10165410, URL https://www.mdpi.com/2076-3417/10/16/5410.

[86] Gillette, D. A., Fryrear, D. W., Gill, T. E., Ley, T., Cahill, T. A., and Gearhart, E. A., "Relation of vertical flux of particles smaller than 10 μm to total aeolian horizontal mass flux at Owens Lake," *Journal of Geophysical Research: Atmospheres*, Vol. 102, No. D22, 1997, pp. 26009–26015. https://doi.org/https://doi.org/10.1029/97JD02252, URL https://agupubs.onlinelibrary.wiley.com/doi/abs/10.1029/97JD02252.

[87] Rajot, J., Alfaro, S., Gomes, L., and Gaudichet, A., "Soil crusting on sandy soils and its influence on wind erosion," *CATENA*, Vol. 53, No. 1, 2003, pp. 1–16. https://doi.org/https://doi.org/10.1016/S0341-8162(02)00201-1, URL https://www.sciencedirect.com/science/article/pii/S0341816202002011.

[88] Macpherson, T., Nickling, W. G., Gillies, J. A., and Etyemezian, V., "Dust emissions from undisturbed and disturbed supply-limited desert surfaces," *Journal of Geophysical Research: Earth Surface*, Vol. 113, No. F2, 2008. https://doi.org/https://doi.org/10.1029/2007JF000800, URL https://agupubs.onlinelibrary.wiley.com/doi/abs/10.1029/2007JF000800.

[89] Marticorena, B., and Bergametti, G., "Modeling the atmospheric dust cycle: 1. Design of a soil-derived dust emission scheme," *Journal of Geophysical Research: Atmospheres*, Vol. 100, No. D8, 1995, pp. 16415–16430. https://doi.org/10.1029/95JD00690.

[90] Gillette, D. A., and Passi, R., "Modeling dust emission caused by wind erosion," *Journal of Geophysical Research: Atmospheres*, Vol. 93, No. D11, 1988, pp. 14233–14242. https://doi.org/https://doi.org/10.1029/JD093iD11p14233, URL https://agupubs.onlinelibrary.wiley.com/doi/abs/10.1029/JD093iD11p14233.

[91] Alfaro, S. C., and Gomes, L., "Modeling mineral aerosol production by wind erosion: Emission intensities and aerosol size distributions in source areas," *Journal of Geophysical Research: Atmospheres*, Vol. 106, No. D16, 2001, pp. 18075–18084. https://doi.org/https://doi.org/10.1029/2000JD900339, URL https://agupubs.onlinelibrary.wiley.com/doi/abs/10.1029/2000JD900339.

[92] Kok, J. F., Mahowald, N. M., Fratini, G., Gillies, J. A., Ishizuka, M., Leys, J. F., Mikami, M., Park, M.-S., Park, S.-U., Van Pelt, R. S., and Zobeck, T. M., "An improved dust emission model – Part 1: Model description and comparison against measurements," *Atmospheric Chemistry and Physics*, Vol. 14, No. 23, 2014, pp. 13023–13041. https://doi.org/10.5194/acp-14-13023-2014, URL http://dx.doi.org/10.5194/acp-14-13023-2014.

[93] Shao, Y., and Lu, H., "A simple expression for wind erosion threshold friction velocity," *Journal of Geophysical Research: Atmospheres*, Vol. 105, No. D17, 2000, pp. 22437–22443. https://doi.org/https://doi.org/10.1029/2000JD900304, URL https://agupubs.onlinelibrary.wiley.com/doi/abs/10.1029/2000JD900304.

[94] Andreotti, B., Claudin, P., Iversen, J. J., Merrison, J. P., and Rasmussen, K. R., "A lower-than-expected saltation threshold at Martian pressure and below," *Proceedings of the National Academy of Sciences*, Vol. 118, No. 5, 2021, p. e2012386118. https://doi.org/10.1073/pnas.2012386118, URL https://www.pnas.org/doi/abs/10.1073/pnas.2012386118.

[95] Patel, M., Rabinovitch, J., and Capecelatro, J., "Eulerian–Lagrangian Simulations of Plume-Induced Sheared Granular beds under Martian Conditions," *AIAA SCITECH 2022 Forum*, 2022. https://doi.org/10.2514/6.2022-2193, URL https://arc.aiaa.org/doi/abs/10.2514/6.2022-2193.

[96] McAlpine, J. D., Koracin, D. R., Boyle, D. P., Gillies, J. A., and McDonald, E. V., "Development of a rotorcraft dust-emission parameterization using a CFD model," *Environmental Fluid Mechanics*, Vol. 10, No. 6, 2010, pp. 691–710. https://doi.org/10.1007/s10652-010-9191-y, URL https://doi.org/10.1007/s10652-010-9191-y.

[97] Jasion, G., and Shrimpton, J., "Prediction of Brownout Inception Beneath a Full-Scale Helicopter Downwash," *Journal of the American Helicopter Society*, Vol. 57, No. 4, 2012, pp. 1–13. https://doi.org/doi:10.4050/JAHS.57.042006, URL https://www.ingentaconnect.com/content/ahs/jahs/2012/00000057/00000004/art00006.

[98] Hardy, B., Rauchenzauner, S., Fede, P., Schneiderbauer, S., Simonin, O., Sundaresan, S., and Ozel, A., "Machine Learning Approaches to Close the Filtered Two-Fluid Model for Gas–Solid Flows: Models for Subgrid Drag Force and Solid Phase Stress," *Industrial & Engineering Chemistry Research*, Vol. 63, No. 18, 2024, pp. 8383–8400. https://doi.org/10.1021/acs.iecr.3c04652, URL https://doi.org/10.1021/acs.iecr.3c04652.

[99] Govindarajan, B. M., and Leishman, J. G., "Predictions of Rotor and Rotor/Airframe Configurational Effects on Brownout

Dust Clouds," *Journal of Aircraft*, Vol. 53, No. 2, 2016, pp. 545–560. https://doi.org/10.2514/1.C033447, URL https://doi.org/10.2514/1.C033447.